An evaluation of factors influencing pore pressure in accretionary complexes: Implications for taper angle and wedge mechanics

Demian M. Saffer[1] and Barbara A. Bekins[2]

Received 10 August 2005; revised 2 December 2005; accepted 13 December 2005; published 4 April 2006.

[1] At many subduction zones, accretionary complexes form as sediment is off-scraped from the subducting plate. Mechanical models that treat accretionary complexes as critically tapered wedges of sediment demonstrate that pore pressure controls their taper angle by modifying basal and internal shear strength. Here, we combine a numerical model of groundwater flow with critical taper theory to quantify the effects of sediment and décollement permeability, sediment thickness, sediment partitioning between accretion and underthrusting, and plate convergence rate on steady state pore pressure. Our results show that pore pressure in accretionary wedges can be viewed as a dynamically maintained response to factors which drive pore pressure (source terms) and those that limit flow (permeability and drainage path length). We find that sediment permeability and incoming sediment thickness are the most important factors, whereas fault permeability and the partitioning of sediment have a small effect. For our base case model scenario, as sediment permeability is increased, pore pressure decreases from near-lithostatic to hydrostatic values and allows stable taper angles to increase from ~2.5° to 8°–12.5°. With increased sediment thickness in our models (from 100 to 8000 m), increased pore pressure drives a decrease in stable taper angle from 8.4°–12.5° to <2.5–5°. In general, low-permeability and thick incoming sediment sustain high pore pressures consistent with shallowly tapered geometry, whereas high-permeability and thin incoming sediment should result in steep geometry. Our model results compare favorably with available data from active accretionary complexes. Active margins characterized by a significant proportion of fine-grained sediment within the incoming section, such as northern Antilles and eastern Nankai, exhibit thin taper angles, whereas those characterized by a higher proportion of sandy turbidites, such as Cascadia, Chile, and Mexico, have steep taper angles. Observations from active margins also indicate a strong trend of decreasing taper angle (from >15° to <4°) with increased sediment thickness (from <1 to 7 km). One key implication is that hydrologic properties may strongly influence the strength of the crust in a wide range of geologic settings.

Citation: Saffer, D. M., and B. A. Bekins (2006), An evaluation of factors influencing pore pressure in accretionary complexes: Implications for taper angle and wedge mechanics, *J. Geophys. Res.*, *111*, B04101, doi:10.1029/2005JB003990.

1. Introduction

[2] At subduction zones, fluid-rich sediments on the incoming oceanic plate are off scraped to form an accretionary wedge or are underthrust with the subducting plate. As the incoming sediments are buried and, in the case of accreted sediments, subjected to lateral tectonic stress, their porosity is reduced from greater than 50% before subduction to less than 15% within 20 km of the trench, and pore fluid is expelled [e.g., *Bray and Karig*, 1985]. The combination of low permeabilities typical of marine sediment and rapid loading rates can drive pore pressures well in excess of hydrostatic [*Shi and Wang*, 1988; *Neuzil*, 1995; *Screaton et al.*, 1990]. Elevated pore pressures, in turn, reduce effective stress, leading to decreased shear strength on faults, and allowing the development of mechanically stable thinly tapered accretionary wedges [e.g., *Hubbert and Rubey*, 1959; *Davis et al.*, 1983].

[3] Numerous detailed studies have been conducted to characterize pore pressure and fluid flow at individual margins [e.g., *Screaton et al.*, 1990; *Wang*, 1994; *Bekins et al.*, 1995; *Saffer and Bekins*, 1998; *Henry*, 2000] and have shown that several factors can influence dewatering rates and pore pressures in accretionary complexes, including sediment and fault permeability, wedge geometry, plate convergence rate, and the rate of porosity loss with depth (a function of sediment matrix compressibility) [e.g., *Bekins and Dreiss*, 1992]. Other work has suggested that the partitioning of sediment between accretion and underthrusting may also play a role in controlling pore pressures [e.g.,

[1]Department of Geosciences, Pennsylvania State University, University Park, Pennsylvania, USA.
[2]U.S. Geological Survey, Menlo Park, California, USA.

0148-0227/06/2005JB003990$09.00

Table 1. Parameters and Ranges of Values Examined in This Study

Parameter	Symbol	Range of Values	Nature of Effect on Pore Pressure
Bulk permeability	k	$k_0 = 10^{-22}$ to $10^{-17.5}$ m^2	controls rate of fluid flow
Decollement permeability	k_d	$k = 10^{-15}$ to 10^{-13} m^2	controls rate of fluid flow
Plate convergence rate	v_p	1–10 cm yr^{-1}	controls fluid source terms
Sediment thickness	—	100–8000 m	controls fluid source terms, drainage path length
Percent sediment accreted	—	10–90%	controls fluid source terms, drainage path length
Surface slope	α	0.5°–9°	controls fluid source terms, drainage path length
Subduction angle	β	fixed at 2°	controls fluid source terms, drainage path length

MacKay et al., 1992; *Polonia et al.*, 1999; *Brown and Westbrook*, 1988]. Although the importance of pore pressures in subduction zones is widely recognized, a systematic, quantitative understanding of the parameters that control pore pressure and of feedbacks between hydrogeology, accretionary margin morphology, and accretionary wedge mechanics is needed.

[4] In this paper, we expand on previous work [*Saffer and Bekins*, 2002] to more completely evaluate the relative importance of factors that control pore pressure and the resulting geometry of subduction-accretion complexes. The factors we consider here include sediment and fault permeabilities, incoming sediment thickness, convergence rate, and partitioning of sediment between accretion and underthrusting (Table 1). By isolating and quantifying the influence of each of these factors on pore pressure, we establish a basic framework for considering observations from active accretionary complexes. Specifically, we use a numerical model of fluid flow in accretionary complexes to (1) conduct a detailed sensitivity study of factors that control spatially and temporally averaged pore pressures, and (2) combine model results with critical taper theory to understand the relative role of each factor in controlling taper angles of accretionary wedges. We then discuss observations from active subduction-accretion complexes in light of our modeling results. Some additional factors that may affect permeability structure and dewatering in accretionary complexes, such as bathymetric relief on the incoming oceanic plate [*Lallemand and Le Pichon*, 1987], complex fault permeability behavior [*Henry*, 2000; *Revil and Cathles*, 2002], feedbacks between wedge geometry, trench sedimentation patterns, and possibly climate [e.g., *Lamb and Davis*, 2003] are not considered here.

1.1. Critical Taper Theory

[5] The movement of large, thin thrust sheets requires a weak basal detachment, maintained by either a low friction coefficient or locally elevated pore pressure [e.g., *Hubbert and Rubey*, 1959; *Chapple*, 1978; *Platt*, 1986]. The critical taper model of accretionary wedges and thrust belts [*Davis et al.*, 1983; *Dahlen*, 1984] treats them as growing, self-similar wedges of deforming sediment, at Coulomb failure throughout. Basal and internal frictional forces are balanced against gravitational forces resulting from the wedge taper angle. Despite its simplicity, this model has been widely applied and had great success in matching observed geometry and pore pressures in active systems [e.g., *Kukowski et al.*, 2001; *Davis and von Huene*, 1987; *Lallemand et al.*, 1994] and is also consistent with the results of "sandbox" experiments [e.g., *Davis et al.*, 1983; *Lallemand et al.*, 1994].

[6] Critical taper theory describes the total taper angle of an actively accreting wedge (expressed as the sum of the surface slope, α, and basal décollement dip, β) as a function of pore pressure ratio (reported as $\lambda = P_f/P_l$, where P_f is fluid pressure and P_l is lithostatic pressure, both referenced to the seafloor) along the basal décollement, λ_b, and within the wedge, λ, coefficients of sliding friction along the basal décollement ($\mu_b = \tan \phi_b$) and within the wedge ($\mu = \tan \phi$), and the densities of water, ρ_w, and bulk sediment, ρ_b. *Davis et al.* [1983] presented an approximate solution for the critical taper of actively accreting wedges corresponding to the lower boundary of the wedge stability field defined by *Dahlen* [1984]:

$$\alpha + \beta = \frac{(1-\lambda_b)\mu_b + \left(1-\frac{\rho_w}{\rho_b}\right)\beta}{\left(1-\frac{\rho_w}{\rho_b}\right) + (1-\lambda)K}, \tag{1a}$$

where

$$K = \frac{\sin\phi}{1-\sin\phi} + \frac{\sin^2\phi_b + \cos\phi_b\left(\sin^2\phi - \sin^2\phi_b\right)^{1/2}}{\cos^2\phi_b + \cos\phi_b\left(\sin^2\phi - \sin^2\phi_b\right)^{1/2}}, \tag{1b}$$

and ϕ and ϕ_b are the angle of internal friction for the wedge material and along the wedge base, respectively. Larger pore pressures, smaller friction coefficients along the décollement, and larger friction coefficients for wedge sediment all lead to smaller taper angles. Wedges with pore pressures in excess of those necessary to maintain a specified critical taper are considered "supercritical" and will undergo gravitational collapse [*Dahlen*, 1984]. Wedges with pore pressures below those required for their critical taper are "subcritical" and will steepen by frontal accretion, reactivation of existing thrust faults, or underplating to achieve a critical taper angle.

1.2. Links Between Taper Angle and Fluid Production

[7] As discussed by *Neuzil* [1995], the generation of pore pressure can be viewed as a response to fundamental factors that fall into two categories: (1) those that affect hydrologic forcing and (2) those that control dissipation of pore pressure. Hydrologic forcing, Γ (typically expressed in units of fluid volume per rock volume per time, with units of T^{-1}), results from geologic processes that act as distributed sources or sinks of fluid. These may represent actual sources of fluid volume (e.g., from hydrocarbon generation or dehydration reactions) or virtual ones that act as pressure sources (e.g., disequilibrium compaction or thermal pressurization). Fluid dissipation is controlled by the combination of bulk hydraulic conductivity (K, in units of L/T) and drainage path length (L). *Neuzil* [1995] examined a wide range of geologic settings and scales, and showed that

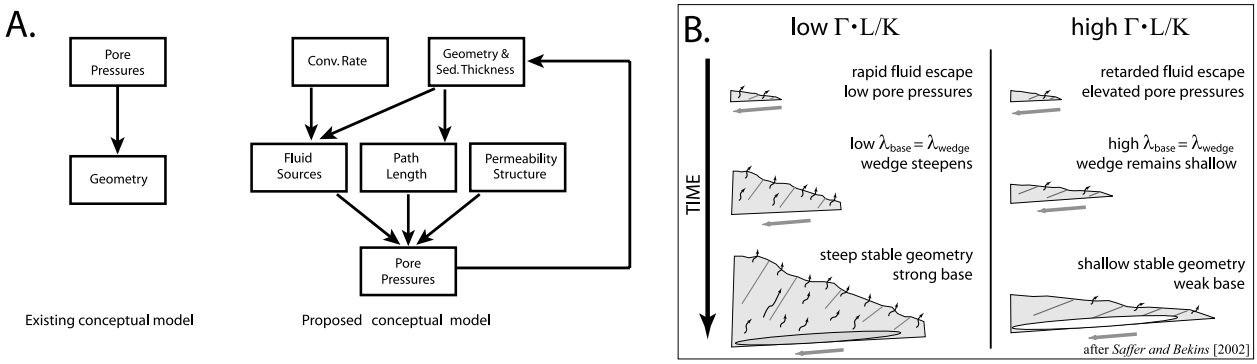

Figure 1. (a) Flowchart showing (left) existing and (right) proposed conceptual models for critically tapered accretionary wedges. The revised model presented here considers pore pressure as the result of a dynamic balance between factors driving fluid source terms (geometry, sediment thickness, and plate convergence rate) and factors that govern fluid escape (permeability and drainage path length). (b) Schematic diagram [after *Saffer and Bekins*, 2002] showing feedback between factors influencing accretionary wedge geometry. Systems characterized by low permeability and/or rapid hydrologic forcing result in shallow taper angles, whereas those characterized by high permeability and/or slow hydrologic forcing are well drained and steeply tapered.

significant fluid overpressures, defined by a hydraulic head gradient of unity, can be expected if $\Gamma > K/L$.

[8] In considering the fundamental processes that drive excess pore pressure, the direct causal relationship between pore pressure ratio (λ) and taper angle is more complicated than implied by equation (1a), because the wedge taper angle actually affects pore pressure by controlling both hydrologic forcing and drainage path length. The dependence of hydrologic forcing on taper angle (and incoming sediment thickness) is evident in considering quantitative descriptions of fluid production from sediment compaction. On the basis of the conservation of solid mass in the sediment matrix and the simplifying assumption of uniformly diverging pathways for accreted sediment packets, compaction-driven fluid source terms, Γ, in a self-similarly growing accretionary wedge are given by the divergence of sediment velocity [e.g., *Screaton et al.*, 1990; *Bekins and Dreiss*, 1992]. Sediment velocity, in turn, depends upon the taper angle, porosity distribution in the wedge, plate convergence rate, and initial incoming sediment height. The resulting fluid sources given as a function of distance landward from the trench, x, and depth beneath the seafloor, z, are [*Bekins and Dreiss*, 1992]:

$$\Gamma(x,z) = \nabla \cdot \mathbf{v}_s = \frac{v_p h}{h + x(\tan\alpha + \tan\beta)} \frac{[1 - n(0,z_0)]}{[1 - n(x,z)]^2} \cdot \left[\frac{\partial n}{\partial x} - \frac{v_z(0,z_0)}{v_p}\frac{\partial n}{\partial z}\right], \quad (2)$$

where $\mathbf{v}_s$ is the sediment velocity vector (L T^{-1}), v_p is convergence velocity (L T^{-1}), h is incoming sediment thickness (L), α and β are surface slope and décollement dip, respectively, n is fractional porosity (a function of x and z), z_0 is the initial depth (L) during accretion of a sediment packet located at (x, z), and v_z is vertical sediment velocity (L T^{-1}; a function of x and z). This formulation is similar to methods developed by others for calculating sediment dewatering rates [*Screaton et al.*, 1990; *Ferguson et al.*, 1993; *Karig*, 1985] and was extended to curved geometry by *Wang* [1994].

[9] The source terms defined in equation (2) drive fluid flow and, in combination with the distribution of hydraulic conductivity, control the development of pore pressures. Steady state pore pressure diffusion accounting for fluid sources is described by

$$\nabla \cdot \left[\left(\frac{k\rho_w}{\upsilon}\right) \cdot (\nabla P - \rho_w g)\right] - Q = 0, \quad (3)$$

where ρ_w is fluid density (M L^{-3}), P is fluid pressure (M L^{-1} T^{-2}), g is gravitational acceleration (L T^{-2}), k is permeability (L^2), υ is dynamic viscosity (M L^{-1} T^{-1}), and Q is a fluid source term (M L^{-3} T^{-1}) driven by the sediment compaction. (Note that Q is related to Γ as defined in equation (2) by $Q = \rho_w\Gamma$.)

[10] On the basis of the strong influence of wedge geometry on hydrologic forcing and thus on resulting fluid pressures, *Saffer and Bekins* [2002] described a conceptual model for accretionary wedges in which the wedge geometry is both a response to the temporally and spatially averaged pore pressure [e.g., *Davis et al.*, 1983] and also one of the main factors that drive pore pressure (Figure 1a). They examined a range of feasible values controlling hydrologic forcing and pore pressure dissipation (Table 1) and concluded that for low permeability or large values of hydrologic forcing, an accretionary complex should maintain high pore pressures and a small taper angle. For high permeability or small values of hydrologic forcing, the complex should be well drained and evolve to a state of high basal shear strength and steep taper angle (Figure 1b). A steep wedge with low permeability drives pore pressures above those required to maintain the initial steep taper angle and will be supercritical. Conversely, a thinly tapered wedge with high permeability will be subcritical. Any change in hydrologic forcing or permeability structure through time by a change in sediment thickness, or incorporation of different sediment type, for example, impacts pore pressure

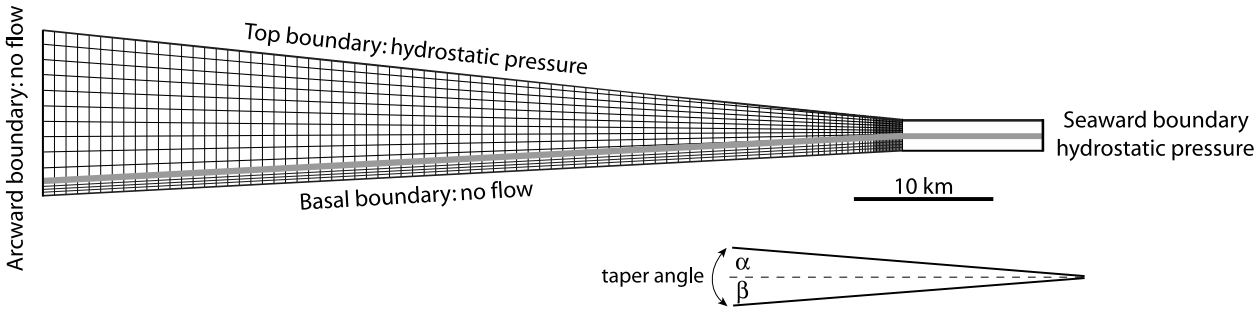

Figure 2. Numerical model domain, boundary conditions, and grid. The grid contains 44,970 elements (46,500 nodes), with 30 rows and 1499 columns. The prism contains 13 rows of elements, the underthrust contains 11, and the décollement consists of 6 closely spaced, higher-permeability elements. The three elements immediately above and below the décollement are also closely spaced. For clarity, the nodes within and surrounding the décollement are not shown, and only every 15th column of nodes and every second row in the underthrust are shown.

and should force the taper angle to adjust until a new dynamic balance is reached [e.g., *Lallemand and Le Pichon*, 1987]. Here, following *Saffer and Bekins* [2002], we consider this important link in evaluating the stability of model wedges by combining simulated pore pressures with the predictions of critical taper theory as discussed below (section 2.2).

2. Methods

2.1. Numerical Model Description

[11] Our model formulation simulates steady state fluid pressures within a cross section perpendicular to the subduction trench (Figure 2). We used the computer code SUTRA [*Voss*, 1984] with modifications made by *Bekins et al.* [1995] to solve the two-dimensional, finite element form of (3). Because the model describes steady state flow, these simulations do not account for changes in pressure or permeability through time. Although there is extensive evidence of transient flow in accretionary complexes [*Carson and Screaton*, 1998], the mechanical analysis of *Davis et al.* [1983] is based on steady state pore pressure. In this study, the results of steady state simulations are used to represent long-term spatial and temporal averages relevant to the maintenance of critical taper angle.

[12] We ran a series of model simulations to calculate steady state pore pressures for a range of surface slopes, bulk and décollement permeabilities, incoming sediment thicknesses, sediment partitioning, and plate convergence rates (Table 1). The cross-sectional model domain contains three regimes: the accretionary prism, the décollement, and the underthrust sediment. The model domain extends from 10 km seaward of the deformation front to 50 km landward and is divided into 44,970 quadrilateral elements defined by 46,500 nodes (Figure 2). Temperatures within the model domain are calculated assuming a steady state conductive thermal regime, using the method of *Ferguson et al* [1993]. We fix the basal heat flux on the incoming plate to be 100 mW/m^2 for all simulations (appropriate for ~15 Ma crust). These temperatures are then used to define fluid properties (density and viscosity) within each model element [*Bekins et al.*, 1995; *Voss*, 1984]. We do not explore the effects of varying age of the incoming plate, but note that in general, higher temperatures will lead to lower fluid density and viscosity, and ultimately to lower pore pressures [e.g., *Spinelli et al.*, 2006]. Direct inputs for the hydrologic model are boundary conditions, compaction-driven fluid sources, sediment velocities (defined following *Bekins and Dreiss* [1992]), temperatures, and permeabilities; outputs from the model include pore pressure distribution and fluid velocities. For a detailed discussion of model inputs, we refer the reader to *Bekins et al.* [1995, and references therein] *Saffer and Bekins* [1998, and references therein].

2.1.1. Boundary Conditions

[13] We assign hydrostatic pressure to the nodes at the seaward boundary of the model domain because changes in the pressure boundary at 10 km from the deformation front have little effect on modeled pressures or flow [*Screaton et al.*, 1990]. Hydrostatic pressures are also specified for nodes at the seafloor (Figure 2). We specify the landward edge of the model as a no-flow boundary, based on the assumption that permeabilities and fluid sources at distances greater than 50 km landward of the deformation front are insignificant. We treat the bottom edge of the model domain as a no-flow boundary, under the assumption that permeability of low-porosity basal sediment is small. The effect of hydrologic communication between sediment and high-permeability underlying ocean crust was explored by *Saffer and Bekins* [1998] for Nankai and shown to have only a small effect on modeled pore pressures and fluid fluxes. The role of basement permeability is not explored further in this paper. However, recent work has shown that basement permeability may be relatively more important with thin sediment sections and steep taper angles [*Matmon and Bekins*, 2006].

2.1.2. Porosities and Compaction-Driven Fluid Sources

[14] Because accretionary wedges grow in a self-similar manner [e.g., *Davis et al.*, 1983], we fix our model coordinate system to the deformation front [e.g., *Screaton et al.*, 1990]. In this framework, sediment enters the accretionary wedge at the deformation front with an initial

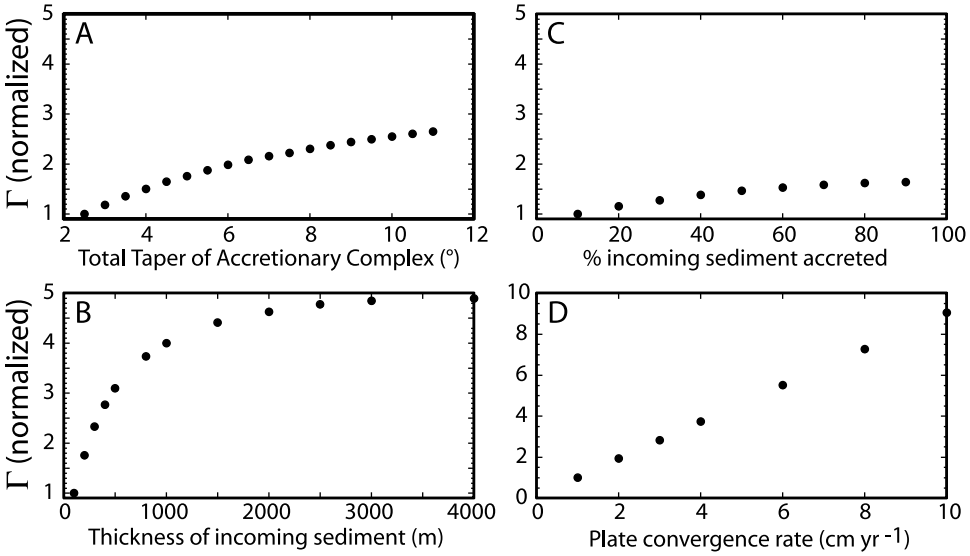

Figure 3. Plot illustrating ratio of average fluid source terms, Γ, to minimum case as a function of (a) total taper angle, minimum case taper angle of 2.5°, (b) incoming sediment thickness, minimum case thickness of 100 m, (c) percentage of incoming sediment that is accreted (minimum case is 10% of sediment accreted), and (d) plate convergence rate (minimum case convergence rate is 1 cm yr^{-1}). All values are averaged over the front 50 km of the accretionary complex.

porosity and dewaters as it is transported arcward with respect to the trench.

[15] We define porosity as a function of depth and distance landward from the subduction trench, following *Bray and Karig* [1985]:

$$n_p(x,z) = 0.60\exp\left[\left(0.24e^{-0.03x} - 0.74\right)z\right], \qquad (4)$$

where z is depth in kilometers below the seafloor, n_p is prism porosity, and x is distance arcward of the deformation front in kilometers. The porosity-depth function is $n_p = 0.60e^{-0.50z}$ at the deformation front and approaches $n_p = 0.60e^{-0.74z}$ with increasing distance arcward. This formulation is consistent with microstructural observations, resistivity anisotropy measurements, and anisotropy of magnetic susceptibility (AMS) data from active wedges, which indicate bulk lateral shortening [*Behrmann and Kopf*, 1993; *Housen et al.*, 1996; *Henry et al.*, 2003].

[16] Drilling and seismic data at a number of accretionary complexes indicate a sharp porosity increase across the décollement [*Hyndman et al.*, 1993a; *Moore et al.*, 2001; *Cochrane et al.*, 1994], attributed to a combination of higher total stress in the wedge and limited drainage in the underthrust. Drilling results show that the underthrust sediment retains anomalously high porosity for its burial depth to at least a few kilometers arcward of the deformation front [e.g., *Screaton et al.*, 2002; *Saffer*, 2003], and seismic reflection data indicate underconsolidated conditions to 20–30 km arcward [*Bangs et al.*, 2004]. On the basis of these data, we assign the same exponential porosity decrease with depth to the underthrust sequence as for the overlying wedge, but specify that at the trench these sediments become underconsolidated with respect to the overlying prism, and remain so for 30 km from the deformation front. Beyond 30 km, porosities again become continuous across the décollement (following *Saffer and Bekins* [1998] and equation (4)).

[17] Compaction fluid sources in the wedge are calculated from the divergence of sediment velocity (equation (2)), assuming conservation of solid mass in the sediment matrix and that time-averaged sediment velocities within the wedge can be approximated as uniformly diverging [e.g., *Bray and Karig*, 1985; *Bekins and Dreiss*, 1992; *Wang*, 1994; *Morgan and Karig*, 1993]. We calculate sediment velocity in a coordinate system fixed at the trench, following *Bekins and Dreiss* [1992] and *Screaton et al.* [1990]. For accreted sediments, velocities are smaller than the convergence rate and decrease with distance arcward, owing to sediment thickening (vertical extension) and porosity loss [e.g., *Bekins and Dreiss*, 1992; *Ferguson et al.*, 1993]. The velocities are a function of basal dip and surface slope, convergence rate, porosity distribution, and sediment thickness (equation (2)). In the underthrust section, sediment velocities are fixed at the convergence rate, and fluid sources are calculated from porosity loss and sediment velocity [*Bekins et al.*, 1995; *Saffer and Bekins*, 1998].

[18] It is clear that from equation (2) geometry is a primary control on the distribution and magnitude of fluid sources [*Bekins and Dreiss*, 1992]. Steeper geometries result in more rapid burial and dewatering, which are concentrated near the wedge toe because the highest dewatering rates occur early in compaction [e.g., *Athy*, 1930]. Lower taper angles result in fluid sources which are of smaller magnitude at the toe, but persist to greater distances from the trench. For a given sediment thickness, an increase in wedge taper from 2.5° to 11° corresponds to a ~270% increase in average fluid sources (Figure 3a). Thickness of the incoming sediment section is also a key control on fluid sources; thicker incoming sediment results in higher total fluid sources (Figure 3b), and more evenly distributed dewatering throughout the system, whereas thinner sec-

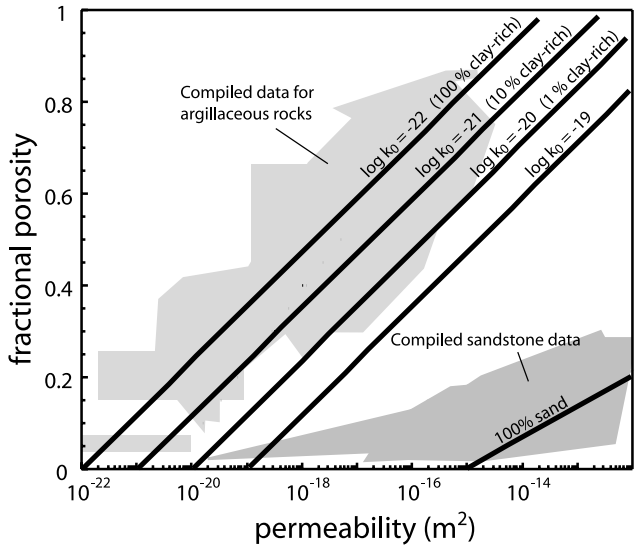

Figure 4. Sediment permeability as a function of porosity. Shaded areas show compiled data for clays and shales [*Neuzil*, 1994] and sands [*Nelson*, 1994]. Lines show a subset of the permeability-porosity relations used in our simulations; each line is also labeled to indicate the percentage mixture of clay and sand that it reflects in the case of layer-normal flow.

tions concentrate dewatering near the wedge toe [*Bekins and Dreiss*, 1992]. This occurs because a thinner sediment section has a higher average porosity and thus loses more porosity overall in the early stages of burial than a thicker one.

[19] The partitioning of the incoming sediment between accretion and underthrusting has a relatively small effect on fluid sources (Figure 3c), due to two competing effects. First, porosity loss with lateral distance from the deformation front in the underthrust section is typically smaller than porosity loss within the overlying accreted material. This acts to decrease the magnitude of fluid sources in the underthrust section relative to the prism, but also to maintain these smaller sources over a larger distance from the deformation front. Second, the underthrust section is buried beneath the prism at the plate convergence rate, whereas the accreted sediment is transported arcward more slowly as it undergoes horizontal compaction. This acts to increase hydrologic forcing in the underthrust relative to the prism. The two effects counteract one another, resulting in only a small increase in fluid source terms as the accreted section increases from 10 to 90% of the total sediment thickness (Figure 3c).

[20] Plate convergence rate also directly affects dewatering rate; increasing the convergence rate from 1 to 10 cm yr^{-1} results in a ninefold increase in hydrologic forcing (Figure 3d). The relationship is not precisely proportional because the sediment velocity decreases as it is buried in the wedge. Because changes in the porosity-depth relationship have been shown to have only a small impact on fluid sources [*Bekins and Dreiss*, 1992], we do not explore its effects in our analyses. We also do not explore the influence of variable clay dehydration rate or clay content here, because fluid source terms from mineral dehydration reactions are typically 1–3 orders of magnitude smaller than those from compaction [e.g., *Bekins et al.*, 1995].

2.1.3. Permeabilities

[21] We define the permeability of model elements by relating log permeability to porosity [e.g., *Nelson*, 1994; *Neuzil*, 1994]:

$$\log k = \gamma n + \log k_0, \tag{5}$$

where k is bulk permeability, n is porosity, γ describes permeability change with porosity, and k_0 is the projected permeability at zero porosity. For simplicity, in exploring the effect of varying bulk permeability in our simulations we only vary the parameter k_0 (Figure 4). This approach effectively simulates a range of bulk permeabilities. We consider a suite of permeability-porosity relations (Figure 4 and equation (5)), for k_0 ranging from $3 \times 10^{-17.5}$ to 10^{-22} m^2, and we fix $\gamma = 8.44$ [*Bekins et al.*, 1995], a value representative of fine-grained sediment [*Neuzil*, 1994]. Fractures or faults that may act as conduits on a local scale are incorporated into single values of bulk permeability for each model element. This approach is justified for large-scale models because discrete fractures act as efficient conduits only when they are closely spaced enough to access fluids from the unfractured sediment matrix. Otherwise, sediment matrix permeability controls the bulk permeability [e.g., *Neuzil*, 1994].

[22] In reality, the effective bulk permeability of sediment (and its anisotropy) is controlled by many factors, including: porosity, grain size, lithology, orientation of sediment layers to the flow field, deformation of strata, effective stress state, and fracturing or faulting. Because the link between permeability and these factors is difficult to quantify rigorously, here we focus on exploring the impact of bulk sediment and fault zone permeability on pore pressures. High bulk permeability may be due to sand-rich lithologies, flow parallel to bedding, and/or dense fracture networks; whereas low bulk permeability corresponds to clay-rich lithologies, flow at high angle to bedding, and/or sparse fracture networks.

[23] We assign the permeability of the décollement separately to represent the effects of channelized fluid flow [e.g., *Screaton et al.*, 1990; *Bekins et al.*, 1995] and consider a range of values from 10^{-13} to 10^{-15} m^2 (Table 1). This is consistent with chemical and thermal observations centered at the depths of major fault zones that indicate focused fluid expulsion [e.g., *Fisher and Hounslow*, 1990; *Kastner et al.*, 1993; *Kimura et al.*, 1997; *Morris et al.*, 2003; *Carson and Screaton*, 1998; *Gieskes et al.*, 1990] and with direct observations of focused discharge where faults outcrop at the seafloor [e.g., *Henry et al.*, 2002; *Ogawa et al.*, 1996]. Focused discharge along faults and high-permeability strata is also inferred from seismic imaging [e.g., *Shipley et al.*, 1994]. Conceptually, elevated fault zone permeability is consistent with fracturing expected as porosity is reduced and rocks begin to experience brittle failure [e.g., *Byrne and Fisher*, 1990; *Moore and Vrolijk*, 1992; *Zhang et al.*, 1993]. Modeling results for many accretionary complexes have also shown that fault permeability greater than that of surrounding sediment is necessary to achieve steady state pore pressures that do not exceed lithostatic values ($\lambda > 1.0$) [e.g., *Screaton et al.*, 1990; *Bekins et al.*, 1995; *Saffer and Bekins*, 1998]. In our work, we consider the effects of a

single permeable zone, but do not explicitly incorporate multiple permeable faults in the accretionary wedge. By incorporating a highly permeable décollement embedded within the accretionary complex, our simulations assess the effects of drainage allowed by a high-permeability conduit connected from depth to the seafloor. Although multiple conduits could yield slightly more efficient drainage (comparable to the effect of higher bulk sediment permeability discussed above), their general effect is captured in our simulations because we consider cases in which both bulk and décollement permeability vary.

2.2. Criteria for Stable Steady State Configurations

2.2.1. Upper Limit for Modeled Pore Pressures

[24] The presence of mineralized veins in exposed accretionary wedge rocks indicates that locally, pore pressures can exceed the overburden stress slightly (i.e., $\lambda \geq 1.0$) [e.g., *Byrne and Fisher*, 1990]. However, such pore pressures cannot be persistent or widespread, because hydraulic fracturing would allow rapid pore pressure diffusion [e.g., *Brown et al.*, 1994]. Furthermore, sustained pore pressures equal to or greater than the lithostatic load would result in a zero effective stress condition, precluding the existence of an accretionary wedge [e.g., *Davis et al.*, 1983]. We therefore consider steady state model simulations that yield pore pressures of $\lambda > 1.0$ to reflect an unrealistic combination of fluid sources and permeabilities.

2.2.2. Maintenance of a Critical Taper Angle

[25] In accordance with the mechanical argument from *Davis et al.* [1983] and described in section 1.1, we adopt the constraint that modeled steady state pore pressures should be consistent with the taper angle. If modeled pore pressures are too high or too low to be consistent with the model domain geometry, we consider the simulation to reflect an unrealistic combination of input parameters [*Saffer and Bekins*, 2002; *Matmon and Bekins*, 2006].

[26] We identify stable combinations of geometry and modeled pore pressure by comparing modeled pore pressures with those predicted by critical taper theory for actively accreting wedges. As is evident from equations (1a)–(1b), the relative strengths of the wedge and base, which depend upon the combination of λ and μ, and λ_b and μ_b, respectively, are the critical parameters controlling taper angle. This raises the problem of defining an appropriate modeled value of λ for the accretionary complex as a whole in order to assess overall wedge stability. In using equations (1a)–(1b) to evaluate critical taper angle, the pore pressure ratio along the wedge base (λ_b) and within the wedge (λ) are usually assumed equal (requiring that $\mu_b < \mu$ in order for a wedge to exist), and bulk density is assumed constant [*Davis et al.*, 1983]. Variability in pore pressure ratio of up to 35% both laterally and with depth can affect wedge taper angle locally by $\sim$1.0–2.0° [e.g., *Zhao et al.*, 1986]. The effect of depth-variable λ is most significant for large taper angles [*Matmon and Bekins*, 2006] and becomes negligible for taper angles <5–6°. Additional studies have also explored the effects of spatially variable bulk density [*Breen and Orange*, 1992] and laterally variable pore pressure ratio [e.g., *Zhao et al.*, 1986], and demonstrate that systematic spatial variations in these quantities can explain the observed convexity at the toes of some accretionary wedges. Although significant spatial variations in pore pressure, cohesion, and bulk density can result in observable changes in wedge taper angle of as much as 0.5–2.0°, these effects are generally secondary in comparison to the effect of overall pore pressure magnitude [e.g., *Breen and Orange*, 1992].

[27] We average simulated values of λ over the front 50 km of the underthrust section and wedge (excluding the upper six nodes) and define stability criteria using equation (1a) assuming $\lambda = \lambda_b$. Because the effects of spatial variability on critical taper angle are secondary to the overall magnitude of pore pressure in controlling taper angle, considering the average value of λ provides a viable first-order assessment of wedge stability for our analysis.

[28] Laboratory data for oceanic sediments and analog mixtures yield values of μ ranging from $\sim$0.3–0.5 over a wide range of lithologies, and generally indicate no pattern of lower friction coefficient for sediments corresponding to those along the décollement, suggesting that μ_b is approximately equal to μ [e.g., *Brown et al.*, 2003; *Kopf and Brown*, 2003; *Logan and Rauenzahn*, 1987]. Values of μ inferred from thrust geometry at modern accretionary complexes are reasonably consistent with the laboratory data and range from 0.36 to 0.62, with most reported values between 0.42 and $\sim$0.5 [*Davis and von Huene*, 1987; *Lallemand et al.*, 1994; *Kukowski et al.*, 2001]. Estimated values of μ_b from fault geometry depend upon assumed pore pressure, and so are generally reported as the effective basal friction coefficient, $\mu_b^* = \mu_b(1 - \lambda_b)/(1 - \lambda)$, with values ranging from 0.15 to 0.35 [*Davis and von Huene*, 1987; *Lallemand et al.*, 1994; *Kukowski et al.*, 2001]. On the basis of these observations, we consider two end-member cases defining critically tapered wedges that span conditions ranging from a relatively strong wedge base having comparable strength to the wedge itself (where $\mu_b = \mu = 0.45$), to a relatively weak base (where $\mu = 0.45$; $\mu_b = 0.30$). Considering an even wider range of friction coefficients broadens the range of stable parameter sets [e.g., *Davis et al.*, 1983] but does not affect the systematic trends we report.

[29] For simplicity, we fix the subduction angle, β, at 2° in our simulations, and allow the surface slope α to vary. For a given total taper angle, fluid sources and thermal structure remain constant, regardless of the individual values of α and β [*Bekins and Dreiss*, 1992; *Ferguson et al.*, 1993]. However, β is a factor in the critical taper stability criterion: With α fixed, steeper values of β allow larger total taper angles for a given pore pressure ratio [e.g., *Davis et al.*, 1983] and thus can extend the range of stable parameter sets defined here to include larger wedge tapers [e.g., *Matmon and Bekins*, 2006].

2.2.3. Spatial Distribution of Pore Pressure

[30] Décollement zones are often characterized by veining, intense brecciation, and collapsed mudstone clasts, which sometimes contain earlier deformation fabrics and are interpreted as evidence of cyclic dilation and collapse [e.g., *Byrne et al.*, 1993; *Ujiie et al.*, 2003]. These observations suggest that in general, the highest pore pressures should be localized in the décollement. Furthermore, in order to account for highly localized strain at the plate boundary, the base of the wedge must be weaker in shear than the surrounding sediment. On the basis of these arguments, we adopt the constraint that the maximum normalized pore pressures occur within the décollement

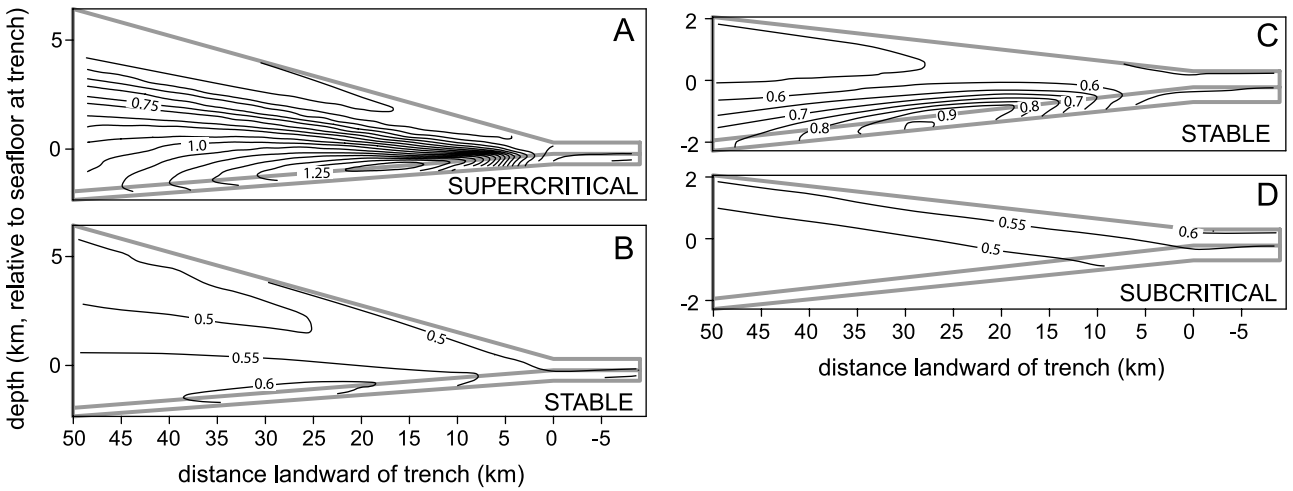

Figure 5. Examples of modeled pore pressure ratio, λ, for (a) $\alpha = 9°$ with $\log k_0 = -20.5$; (b) $\alpha = 9°$ with $\log k_0 = -19.5$; (c) $\alpha = 3.5°$ with $\log k_0 = -20.5$; and (d) $\alpha = 3.5°$ with $\log k_0 = -19.5$. In Figures 5b and 5c, the steep wedge with high permeability and shallow wedge with low permeability both result in simulated pore pressures that yield stable wedges. In Figure 5a, the steep wedge with low permeability leads to extremely large values of $\Gamma \cdot L/K$ and pore pressures well above lithostatic, and it is supercritical. In Figure 5d, the shallow wedge with high permeability results in a small value of $\Gamma \cdot L/K$ and low pore pressures, and it is subcritical.

and underthrusting sediments, along a significant portion of the model length.

3. Modeling Results

[31] Figure 5 shows example contour plots of the normalized pore pressures to illustrate the range of cases obtained with the model. Results from two steep taper angle and two shallow taper angle prisms with contrasting low and high bulk permeabilities are shown. The simulated pore pressures for the shallow wedge with low permeability and the steep wedge with high permeability both yield stable wedges, meaning that modeled values of λ are consistent with their geometry as predicted by critical taper theory (Figures 5b and 5c). In contrast, the steep wedge with low permeability leads to pore pressures well in excess of those consistent with its taper angle (and also well above lithostatic), and is thus classified as supercritical (Figure 5a). Similarly, the shallow wedge with high permeability results in pore pressures well below those required for its taper angle, and is therefore subcritical (Figure 5d).

[32] We use this approach to explore the range of parameters that result in stable versus unstable wedges. To define the sensitivity of pore pressure to each model variable, we define a ''base case'' scenario in which the other model parameters are fixed. For the simulations shown in Figures 6a–6e, unless otherwise noted, subduction angle (β) is held constant at 2°, $k_0 = 10^{-20}$ m^2, décollement permeability is 10^{-15} m^2, $v_p = 4$ cm yr^{-1}, and the incoming sediment section is 1000 m thick, with 500 m accreted. We present the results of a comprehensive sensitivity analyses by plotting modeled pore pressure ratio, λ, as a function of each model variable: bulk permeability, décollement permeability, incoming sediment thickness, sediment partitioning, and plate convergence rate (Figures 6a–6e). Each point in Figures 6a–6e represents a single steady state model simulation; each curve represents a suite of model simulations obtained by varying the taper angle while holding the labeled parameter fixed. The difference in modeled pore pressure between curves indicates the sensitivity of pore pressure to the parameter.

[33] For a given set of model inputs, simulated pore pressures may range from near-hydrostatic to near-lithostatic values as the model domain taper angle is increased (e.g., Figure 6a, curve for $k_0 = -20.5$). This occurs because more steeply tapered model geometries drive larger fluid sources (e.g., Figure 3a), and are characterized by longer drainage path lengths. The solid and dashed curves in Figures 6a–6e show stable taper angles defined by equations (1a)–(1b) as a function of pore pressure ratio, λ, for friction coefficients $\mu_b = \mu = 0.45$ and $\mu_b = 0.30$; $\mu = 0.45$, respectively. (Note that each stability curve corresponds to the lower curve of *Dahlen* [1984] for separate choices of μ_b and μ.) We consider the area between the curves to reflect a feasible combination of parameters. With other simulation parameters fixed, a range of model domain taper angles from 2.5° to 11° may result in pore pressures which define a subcritical wedge for small taper angles, a stable wedge for moderate taper angles, and a supercritical wedge for large taper angles (Figures 6a–6e). We report the range of stable taper angles defined in Figures 6a–6e as a function of bulk permeability (Figure 7a), décollement permeability (Figure 7b), sediment thickness (Figure 7c), sediment partitioning (Figure 7d), and plate convergence rate (Figure 7e).

3.1. Effect of Permeability Structure on Pore Pressures

[34] Sediment bulk permeability has a strong effect on simulated pore pressure. As k_0 is decreased from 3×10^{-19} m^2 to 3×10^{-22} m^2, simulated values of λ increase from 0.52 (hydrostatic) to 0.77 for models with $\alpha = 0.5°$ ($\alpha + \beta = 2.5°$), and from 0.53 to $\gg$1.0 for models with $\alpha = 9°$ ($\alpha + \beta = 11°$) (Figure 6a). For values

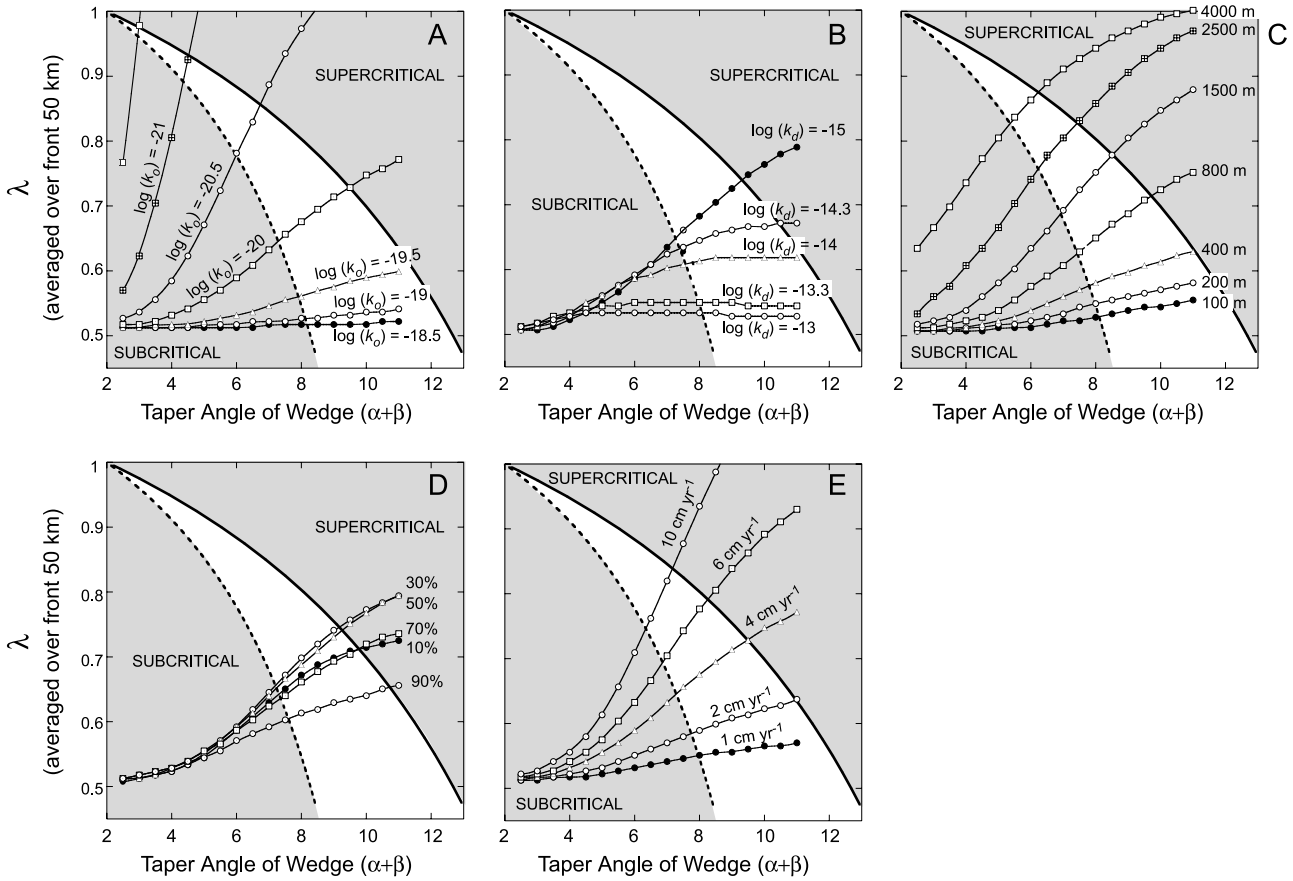

Figure 6. Results of pore pressure sensitivity analysis, showing total taper angle of accretionary wedges ($\alpha + \beta$) versus modeled pore pressure ratio (λ) averaged over the front 50 km of the complex. Dots represent individual steady state model results. Model simulations are for the "base case" described in the text except for the individual parameter explored in each panel. Solid and dashed lines show critically tapered coulomb wedges for a strong ($\mu_b = \mu = 0.45$) and weak ($\mu_b = 0.3$; $\mu = 0.45$) décollement, respectively. Taper angle versus simulated λ is shown for varying (a) bulk permeability; (b) decollement permeability; (c) thickness of incoming sediment; (d) percentages of sediment accretion; and (e) plate convergence rate.

of $k_0 > 10^{-19}$ m^2, pore pressures tend toward hydrostatic values regardless of model geometry. Consequently, the taper angles for which modeled pore pressures fall in the stable field decrease from 8–12.5° to <2.5° with decreasing k_0 (Figures 6a and 7a). For high-permeability simulations, stable taper angles are high and span a range from 8° to 12.5°. As permeability is decreased (and modeled pore pressure increases), the range of critical taper angles defined by our criteria narrows. This is a direct result of the critical taper solution [*Davis et al.*, 1983], in which the importance of friction coefficient diminishes with increased pore pressure (equations (1a)–(1b)).

[35] Modeled pore pressures are less sensitive to décollement permeability than to bulk permeability (Figure 6b). However, conduit permeability does affect pore pressures; in particular, low décollement permeability can lead to nearly undrained conditions in the underthrust section, which dewaters primarily upward to the higher-permeability décollement [e.g., *Carson and Screaton*, 1998; *Le Pichon et al.*, 1993]. High conduit permeability (>5 × 10^{-14} m^2) results in pore pressures that are close to hydrostatic (λ = 0.52) regardless of model geometry, whereas a décollement permeability of 10^{-15} m^2 results in pore pressures ranging from hydrostatic for models with $\alpha = 0.5°$, to $\lambda = 0.79$ for models with $\alpha = 9°$ (Figure 6b). Décollement permeability may affect critical taper, but the strength of its effect depends on bulk permeability. For our base case (k_0 = 10^{-20} m^2), increasing décollement permeability from 10^{-15} m^2 to 10^{-13} m^2 increases stable taper angle only slightly, from 7.4–9.7° to 8.3–12.7° (Figure 7b). For lower bulk permeability (k_0 = 10^{-21} m^2) stable taper angle increases from 4.4–4.6° to 8.1–12.6° over the same range of decollement permeability (Figure 7b). Pore pressures are more sensitive to décollement permeability if matrix permeability is low, because the low bulk permeability limits drainage from sediment near the base of the accreted wedge and in the underthrust section. These results are consistent with those of *Screaton et al.* [1990], who found high sensitivity to decollement permeability in the northern Antilles complex where bulk permeability is low.

[36] Interestingly, the sensitivity of pore pressure to décollement permeability is highest for large taper angles

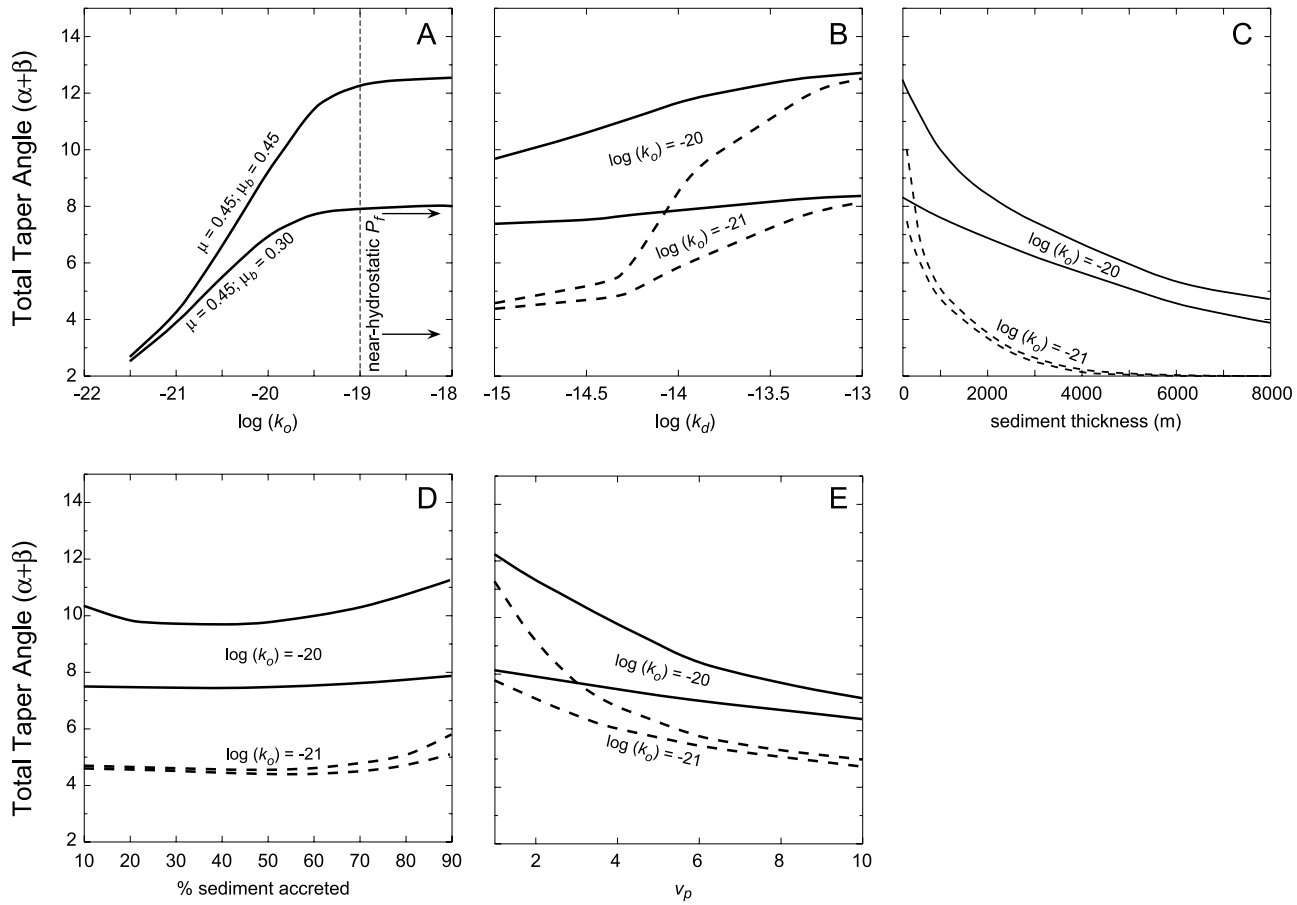

Figure 7. Stable total taper angles ($\alpha + \beta$) identified using the criteria described by equations (1a)–(1b) and shown in Figure 6, plotted as a function of (a) permeability intercept (log k_0); (b) decollement permeability; (c) incoming sediment thickness; (d) sediment partitioning between accretion and underthrusting; and (e) plate convergence rate. The curves for each scenario indicate the range of stable taper angles consistent with end-member strong (solid lines) and weak (dashed lines) décollements shown in Figure 6. In Figures 7b–7e, results are shown for values of log $k_0 = -20$ (solid lines) and -21 (dashed lines).

and becomes negligible for taper angles <4° (Figure 6b). The impact of a high-permeability conduit is amplified in thicker, steeper complexes, because it shortens the drainage path length for sediment in the underthrust section and at the base of the accreted prism. In shallowly tapered wedges, a high-permeability conduit has a smaller effect because the drainage path length for all sediment is short.

3.2. Effect of Sediment Thickness and Partitioning on Pore Pressures

[37] The thickness of incoming sediment has a pronounced effect on pore pressure (Figure 6c). As sediment thickness increases from 100 m to 8000 m, modeled pore pressures increase from $\lambda = 0.52$ (hydrostatic) to $\lambda = 0.85$ for models with $\alpha = 0.5°$, and from $\lambda = 0.56$ to $\lambda \gg 1.0$ for models with $\alpha = 9°$. For our base case of $k_0 = 10^{-20}$ m^2, taper angles for which modeled pore pressures fall into the stability field decrease from 8.25–12.4° to 3.9–4.8° (Figures 6c and 7c). With lower bulk permeability ($k_0 = 10^{-21}$ m^2), stable taper angles range from 7.5–10° for a 100-m-thick section to 2° for thicknesses >4000 m (Figure 7c). Notably, even for high permeabilities characteristic of a sand-rich lithology, a thick sediment section can drive pore pressures to near-lithostatic values. As the model taper angle is increased, the sensitivity of pore pressure to sediment thickness changes slightly (spacing of curves in Figure 6c), and only for thicknesses <1500 m.

[38] The strong sensitivity of pore pressure to sediment thickness is due to three factors: (1) fluid sources over the front 20–40 km of the complex increase with sediment thickness [*Bekins and Dreiss*, 1992] (Figure 3b), (2) sediment thickness controls drainage path length, and (3) thicker sediment sections result in lower porosities, and thus lower permeabilities, within the model domain.

[39] The partitioning of sediment between accretion and underthrusting has a relatively small effect on pore pressures. Pore pressures are hydrostatic for all models with $\alpha = 0.5°$, regardless of the amount of sediment accreted (Figure 6d). As model geometry is steepened to $\alpha = 9°$, pore pressures are highest ($\lambda = 0.80$) for nearly equal partitioning (30–50% accreted), and are only slightly lower when most of the incoming section is either

accreted ($\lambda = 0.66$) or underthrust ($\lambda = 0.72$). Consequently, partitioning of sediment between accretion and underthrusting has a small effect on stable taper angle (Figure 7d).

3.3. Effect of Plate Velocity on Pore Pressures

[40] For our base case scenario and a plate convergence rate of 1 cm yr^{-1}, pore pressures range from hydrostatic for models with a 2.5° taper angle, to a maximum value of $\lambda = 0.57$ for an 11° taper angle. In contrast, for a convergence rate of 10 cm yr^{-1}, modeled pore pressures range from hydrostatic to $\lambda > 1.0$ (Figure 6e). Correspondingly, as v_p is increased from 1 to 10 cm yr^{-1}, the range of taper angles for which modeled pore pressures fall in the stable field decreases from 8.1–12.2° to 6.5–7° (Figure 7e). For lower bulk permeability ($k_0 = 10^{-21}$ m^2), the field of stable taper angles narrows and ranges from 7.8–11.3° to 4.7–5° (Figure 7e). Simulated pore pressures are sensitive to plate convergence rate because it partly controls the burial and accretion rate, and thus the resulting compaction-driven fluid sources (equation (2) and Figure 3d) [*Saffer and Bekins*, 2002].

4. Discussion

4.1. Comparison to Active Accretionary Systems

[41] Our modeling results support the idea that pore pressure can be related to the combination of Γ, L, and K [*Neuzil*, 1995]. In his analysis, *Neuzil* [1995] showed that for values of $\Gamma \cdot L/K > 1$, significant overpressures (corresponding to a head gradient of $dh/dl = 1$) should be expected. To evaluate the applicability of this analysis to accretionary complexes, we consider representative values of Γ, L, and K for our model simulations, and then plot modeled values of normalized pore pressure as a function of the quantity $\Gamma \cdot L/K$ (Figure 8). We report simulated pore pressures using the excess pore pressure ratio λ^* (where $\lambda^* = (P - P_h)/(P_l - P_h)$; $\lambda^* = 0$ for hydrostatic pore pressure and $\lambda^* = 1$ for lithostatic pore pressure) [*Shi and Wang*, 1988], because it accounts for the pore pressure in excess of hydrostatic, whereas the pore pressure ratio λ (where $\lambda = P_h/P_l$) varies even for hydrostatic pore pressure, depending upon the average sediment bulk density. We define Γ as the average fluid source term within the underthrusting sediment between 22 and 28 km from the trench, L as the path length upward to the décollement from the center of the underthrusting sediment column and along the décollement to the trench, and K as the harmonic mean of element-wise hydraulic conductivities along the path of length L. In our model domains, the average bulk density of the sediment column varies from 2140 to 2510 kg m^{-3}; as a result, a unit head gradient ($dh/dl = 1$) corresponds to values of λ^* ranging from 0.70 to 0.92.

[42] For the full range of taper angles, sediment thicknesses, and permeabilities we investigated, modeled pore pressures corresponding to $dh/dl \geq 1.0$ are generated in almost all cases where $\Gamma \cdot L/K > 1$, consistent with *Neuzil*'s [1995] result (Figure 8). Furthermore, our simulations exhibit a trend of systematically increasing pore pressure, with small overpressures beginning at values of $\Gamma \cdot L/K$ as low as ~0.01 (Figure 8). Although such a direct scaling of overpressure with $\Gamma \cdot L/K$ has not been investigated in detail previously, it is consistent with the conceptual model that overpressure is dynamically controlled by the combination of fluid sources, hydraulic conductivity, and drainage path length.

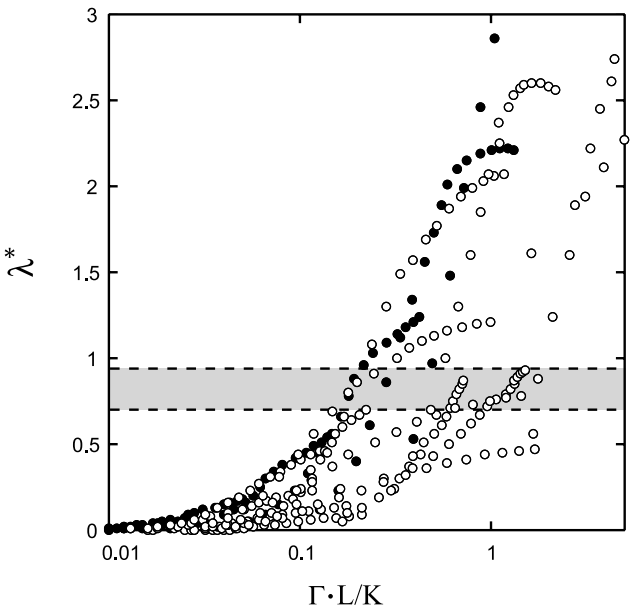

Figure 8. Plot showing relationship between the quantity ($\Gamma \cdot L/K$) versus simulated pore pressure ratio (λ^*) for model runs with varying k_0 (solid circles) and with varying incoming sediment thickness and plate convergence rate (open circles). Gray shaded region shows range of values for λ^* corresponding to $dh/dl = 1$ in our models, defined by $\lambda^* = P_h/(P_l - P_h)$.

[43] Our results indicate that the primary factors in controlling pore pressure in accretionary complexes are sediment permeability, sediment thickness, and plate convergence rate. With a limited number of natural examples, it is not straightforward to isolate the effects of individual parameters and rigorously test our models by comparison with active accretionary complexes. In addition, the incoming sediment section has been drilled and characterized in detail at only a small number of active subduction zones. Direct comparison is also complicated because in many instances the parameters are linked and have competing effects. For example, sediment thickness has been observed to vary inversely with convergence rate (slower convergence is strongly correlated with thicker sediment sections, whereas faster convergence is correlated with thinner sediment sections) [e.g., *Clift and Vannucchi*, 2004]. In this case, the two linked factors have competing effects: thinner sediments tend to drive lower pore pressures, but faster convergence drives higher pore pressures. Thicker sediments are also commonly associated with higher deposition rates, a predominance of silty or sandy turbidites, and presumably higher permeability [e.g., *Brown and Westbrook*, 1988; *Underwood and Bachman*, 1982], although it is important to note that this is not always true [*Underwood*, 2006]. In this case, the two factors should again exhibit competing effects: thicker sediments tend to drive higher pore pressures, but a higher permeability tends to result in lower pore pressures.

Table 2. Summary of Data From Drilling at Active Accretionary Complexes Shown in Figure 9

Margin	α	β	Sediment Thickness, m	v_p, cm yr^{-1}	Percent of Incoming Section Dominated by Muds and Clays	k From Inverse Modeling, m^2	Data Sources[a]
Northern Antilles	1 ± 0.25°	2 ± 0.25°	700	2.8	90 ± 6	7×10^{-22} to 3.4×10^{-20}	1, 2, 3
Nankai (Muroto)	1.5 ± 0.3°	2.5 ± 0.3°	~1000	6.5	82 ± 7	3.5×10^{-20} to 4.5×10^{-19}	4, 5
Nankai (Ashizuri)	5.0 ± 0.5°	4.0 ± 0.5°	~1300	6.5	50 ± 22	—	4
Northern Cascadia	5.5 ± 0.5°	3.5 ± 0.5°	2500	3.7	60 ± 17	5.6×10^{-19} to 1.4×10^{-18}	6, 7, 8, 9
Eastern Aleutian	2 ± 1°	3 ± 1°	≥1500	6.5	66 ± 30	—	6, 10
Mexico (DSDP Leg 66 area)	8.5 ± 1°	7.5 ± 1.5°	670–800	8.5	26 ± 5	—	11, 12

[a]Sources are 1, *Mascle et al.* [1988]; 2, *Dixon et al.* [1998]; 3, *Bekins et al.* [1995]; 4, *Moore et al.* [2001]; 5, *Saffer and Bekins* [1998]; 6, *Kulm et al.* [1973]; 7, *Westbrook et al.* [1994]; 8, *Wang* [1994]; 9, *Giambalvo et al.* [2000]; 10, *Davis and von Huene* [1987]; 11, *J. C. Moore et al.* [1982]; and 12, *Watkins et al.* [1981].

[44] In light of these limitations, we test our model by comparing the systematic relationships predicted by our sensitivity analysis with (1) available data from drilling in active subduction-accretion complexes (Table 2), (2) inverse modeling results from detailed studies of individual accretionary complexes, and (3) data from geophysical studies that constrain sediment facies and thickness for a larger number of margins (Table 3). In all cases, we evaluate whether existing data are consistent with our model results.

[45] Many subduction complexes characterized by margin wedges extending to the trench are nonaccretionary, such as those offshore of Costa Rica, Guatemala, northern Japan, and Nicaragua [e.g., *Kimura et al.*, 1997; *von Huene and Lallemand*, 1990; *Vannucchi et al.*, 2001]. Because these complexes are not actively accreting, our model results are not applicable. Other areas are characterized by long-term tectonic erosion [e.g., *Clift and Vannucchi*, 2004], but have a narrow modern actively deforming wedge [e.g., *Moran-Zenteno et al.*, 1996; *McMillen et al.*, 1982; *Lallemand et al.*, 1994]. Because these areas (e.g., Mexico, Chile) are characterized by modern active accretion, critical taper theory is applicable and we include them in our discussion.

[46] In general, lithology (and thus permeability) have been sampled by drilling and are best documented at margins characterized by thin (<~3 km) incoming sediment sections. These margins should more clearly exhibit the effect of sediment permeability on pore pressure, because large variations in sediment thickness do not obscure its effects [e.g., *Saffer and Bekins*, 2002]. At margins characterized by thick sediment sections, the effect of permeability is less well documented, and is difficult to isolate from the effects of sediment thickness. However, for all thick (>~3 km) sediment sections reported in previous work, the incoming sediments are primarily composed of turbidites, with very little hemipelagic or pelagic material (Table 3 and references therein). Thus, in these examples, the smaller variability in sediment lithology allows us to evaluate the effects of sediment thickness. Below, we discuss (1) the role of permeability by focusing on those margins with thinner sections, where variability in lithology is greater and in which the effects of permeability are not obscured by the effects of sediment thickness; and (2) the role of sediment thickness by focusing on margins with thicker sediment sections, in which lithology is apparently less variable.

4.1.1. Effects of Permeability

[47] Formation-scale permeability is generally not well known in accretionary complexes, due to partial penetration and recovery of the sedimentary section in many cases, and a lack of laboratory permeability measurements and in situ tests at high spatial resolution down section. The only data set that is both consistently available from drilling and related to bulk sediment permeability is core

Table 3. Summary of Data From Active Accretionary Complexes Shown in Figure 10

Margin	Notation in Figure 10	Thickness, m	Taper Angle, deg	Data Sources[a]
Mexico	MX	500	16	1, 2
Java	JA	550	7.9	2, 3
Northern Antilles	NA	700	3	4, 5, 6
Eastern Aleutian (160°W)	AL	925	9.2	7
Nankai (Muroto)	MUR	1000	4	8, 9
Nankai (Ashizuri)	ASH	1100	9	8
Central Sumatra	CS	1300	7.1	2, 3, 10, 11
Sunda	SU	1800	5.9	12
Chile	CH	2000	13.5	13, 14
Nicobar	NI	2300	5.9	3
Eastern Aleutian (148–150°W)	EA	2500	5	15
Northern Cascadia	NC	2500	9	16
Central Aleutian (172–176°W)	CA	2950	8	17
Southern Cascadia	SC	3000	5.7	18, 19
Andaman	AN	4000	3.5	2, 3
Luzon	LU	4300	4.7	20, 21
Burma	BU	6000	3.5	2, 3
Southern Antilles	SA	6300	3.6	22, 23
Makran	MA	7000	2.9	24, 25, 26

[a]Sources are 1, *McMillen et al.* [1982]; 2, *J. C. Moore et al.* [1982]; 3, *Moore et al.* [1980]; 4, *Westbrook* [1982]; 5, *Westbrook et al.* [1988]; 6, *Mascle et al.* [1988]; 7, *Stevenson et al.* [1983]; 8, *Moore et al.* [2001]; 9, *Gulick et al.* [2004]; 10, *Karig et al.* [1980]; 11, *Schlüter et al.* [2002b; 12, *Kopp et al.* [2001]; 13, *Polonia et al.* [1999]; 14, *Laursen et al.* [2002]; 15, *Davis and von Huene* [1987]; 16, *Westbrook et al.* [1994]; 17, *McCarthy and Scholl* [1985]; 18, *Gerdom et al.* [2000]; 19, *Flueh et al.* [1998]; 20, *Karig and Sharman* [1975]; 21, *Hayes and Lewis* [1984]; 22, *Brown and Westbrook* [1988]; 23, *Lallemand et al.* [1994]; 24, *Schlüter et al.* [2002a]; 25, *Minshull and White* [1989]; and 26, *Kukowski et al.* [2001].

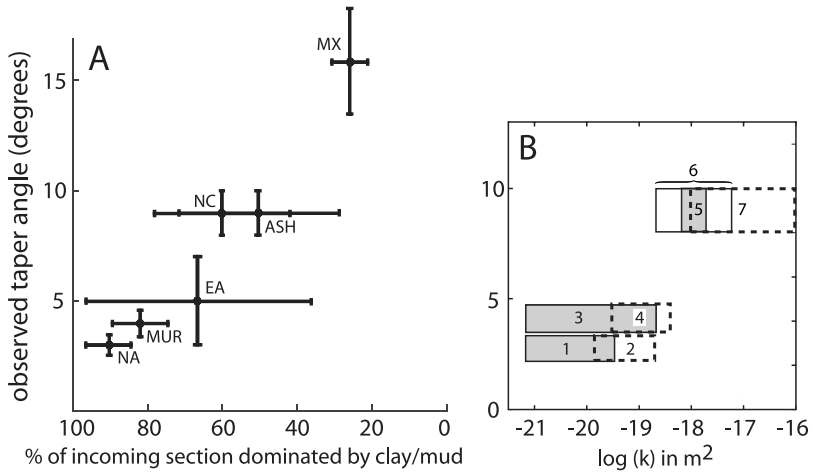

Figure 9. (a) Taper angles of active subduction-accretion complexes where the incoming sediment section has been sampled by drilling, plotted as a function of lithology as taken from visual core descriptions (VCDs) and determined by caliper measurements, and as summarized in Table 2. Horizontal error bars indicate uncertainty in lithology and vertical error bars indicate along-strike variations in taper angle. NA, northern Antilles; MUR, Nankai Muroto; EA, eastern Aleutians; NC, north Cascadia; ASH, Nankai Ashizuri; MX, Mexico. (b) Plot of taper angle versus permeability determined from direct measurements and site-specific inverse modeling studies. Permeability estimates are from (1) inverse modeling of the northern Antilles [*Bekins et al.*, 1995], (2) measurements on core samples from the northern Antilles [*Taylor and Leonard*, 1990], (3) inverse modeling of eastern Nankai [*Saffer and Bekins*, 1998], (4) measurements on core samples from eastern Nankai [*Taylor and Fisher*, 1993], (5) inverse modeling of northern Cascadia [*Wang*, 1994], (6) data from distal hemipelagic sediments and turbidites offshore Cascadia [*Giambalvo et al.*, 2000], and (7) a summary of data for Cascadia [*Carson and Westbrook*, 1995]. For inverse model permeability estimates and the direct measurements of *Taylor and Fisher* [1993] and *Giambalvo et al.* [2000], the range of permeabilities shown is for a range of porosities from 10 to 30%, using the permeability-porosity expression from each detailed study. For direct measurements from northern Antilles, the range shown represents the full range of measured values.

lithostratigraphy. To test if our model is consistent with the characteristics of active accretionary complexes, we use the percentage of fine-grained sediment in the incoming sediment section (mud- and clay-dominated) as a proxy for permeability. This approach compares the relative differences, but not absolute magnitudes, of effective sediment permeability among active systems. We define the percentage of fine-grained material by summing the thickness of mud- and clay-rich sediment described in Deep Sea Drilling Project (DSDP) and ODP visual core descriptions (VCDs), and dividing this sum by the total recovered sediment thickness (Table 2). The minimum and maximum errors in this estimate are based on the amount of drilled but unrecovered sediment; all unrecovered sediment is assumed to be sand to obtain the minimum clay percentage estimate, or clay in the case of the maximum estimate. Error bars are large in some cases, owing to low core recovery. At the northern Antilles and Nankai subduction zones, recovery from ODP drilling has been high, and thus errors in estimating lithologic composition are small.

[48] In cases where coring was discontinuous or stratigraphic units were only partially penetrated, lithostratigraphic units are defined by a combination of drilling and seismic reflection [e.g., *J. C. Moore et al.*, 1982]. In such cases, the core lithology and uncertainty within each stratigraphic unit are assumed constant with depth and the same as the drilled portion. At the Mexico, eastern Aleutian, and Cascadia margins, we combined data from reference sites drilled into proximal trench turbidites (sites 487, 180, and 888) with data from distal fan sections drilled through to basement (sites 486, 178, and 174) to generate composite stratigraphic columns. At Cascadia Site 888, the recovery rate was low, but caliper logs allowed identification of unrecovered sandy intervals [*Westbrook et al.*, 1994].

[49] Existing data from drilling are consistent with our model, which predicts steeper critical taper angles for accretionary complexes composed of coarser-grained (presumably higher-permeability) sediment, and shallower taper angles for complexes dominated by fine-grained sediment (Figure 9a). Summarized below are six systems representing a progression from lowest to highest taper angle and lowest to highest permeabilities. Systems dominated by low-permeability, fine-grained pelagic and hemipelagic sediment, such as northern Antilles [*Mascle et al.*, 1988; *Zwart et al.*, 1997; *Moore and Biju-Duval*, 1984] and eastern Nankai (termed the Muroto transect) [*Moore et al.*, 2001; *Underwood et al.*, 1993; *Taira et al.*, 1992] maintain shallow taper angles of $\sim 2.7^\circ$ and $\sim 4^\circ$, respectively. Those characterized by high-permeability, coarse-grained terrigenous sediment, such as Mexico [*J. C. Moore et al.*, 1982; *McMillen et al.*, 1982] and northern Cascadia [*Westbrook et al.*, 1994; *Underwood*, 2002, 2006] maintain steep taper angles of $\sim 16^\circ$ and $\sim 8-10^\circ$, respectively. Although the plate convergence rate ranges from 2.8 to 7.0 cm/yr in these

examples, variation over the observed range should have a second-order effect on taper angle when compared with variation in permeability, based on the results of our sensitivity analysis (Figure 7e) [see also *Saffer and Bekins*, 2002].

[50] The northern Antilles accretionary wedge is dominated by a pelagic, clay-rich incoming sediment section approximately 700 m thick and is shielded from terrigenous sediment derived from the South American continent by a basement high, the Tiburon Rise [*Mascle et al.*, 1988; *Shipley et al.*, 1995; *Brown and Westbrook*, 1988]. This clay-rich section is characterized by high compressibility and low permeability [e.g., *Zwart et al.*, 1997; *Taylor and Leonard*, 1990]. The plate convergence rate is $\sim$2.8 cm yr^{-1} [*Dixon et al.*, 1998]. The northern Antilles accretionary wedge is characterized by a shallow taper angle of $\sim$2.7° [*Westbrook et al.*, 1988; *Speed et al.*, 1984; *Westbrook et al.*, 1984]. High pore pressures are inferred from the wedge geometry [e.g., *Davis*, 1984], as well as from porosity data collected by drilling [e.g., *Moore and Tobin*, 1997; *Saffer*, 2003].

[51] The eastern Nankai (Muroto) accretionary complex is characterized by a $\sim$1000-m-thick, dominantly hemipelagic incoming sediment section, with some intercalated ash layers [*Moore et al.*, 2001]. The plate convergence rate has been estimated at 4.0 cm yr^{-1} on the basis of plate models [*Seno et al.*, 1993], and more recently at 5.5–6.5 cm yr^{-1} on the basis of GPS data [*Ito et al.*, 1999; *Miyazaki and Heki*, 2001]. As predicted for complexes dominated by fine-grained (and thus low-permeability) sediment, the taper angle of the eastern Nankai wedge is shallow, at $\sim$4° [*Moore et al.*, 1990; *Ashi and Taira*, 1992]. In comparison, the taper angle of the western Nankai accretionary wedge (termed the Ashizuri transect), located $\sim$100 km to the southwest, is 8–10° [e.g., *Moore et al.*, 2001; *Karig*, 1986]. The incoming sediment section at western Nankai is similar to that along the Muroto transect but contains a $\sim$300-m-thick Miocene sandy turbidite sequence not seen to the east [*Moore et al.*, 2001; *Underwood*, 2006], and which probably results in a higher formation-scale permeability. Numerical models of fluid flow within the western Nankai accretionary complex that explicitly include the effects of high-permeability turbidites within the underthrust section yield pore pressures consistent with the steeper taper angle there [*Saffer*, 2002].

[52] The eastern Aleutian accretionary complex in the area drilled during DSDP Leg 18 is characterized by a >1500-m-thick incoming sediment section, composed of a $\sim$780-m-thick trench turbidite facies (penetrated at DSDP Site 180) underlain by a hemipelagic section that is continuous over several 100s of km and thought to be representative of the Alaskan abyssal plain (penetrated at DSDP Site 178) [*Kulm et al.*, 1973]. Both units are generally mud- and clay-dominated, with thin zones of silt and fine sand. Core recovery at both sites was low, resulting in large uncertainty in the lithostratigraphy (Figure 9a). The plate convergence rate is 6.5 cm yr^{-1}, and the taper angle along the drilled transect is 3–7° [*Davis and von Huene*, 1987; *Moore et al.*, 1991].

[53] The Cascadia accretionary prism offshore Vancouver, Canada, is characterized by a $\sim$2500-m-thick incoming sediment section [*Hyndman et al.*, 1993b; *Westbrook et al.*, 1994]. The uppermost $\sim$600 m of the $\sim$1500-m-thick proximal fan facies penetrated by drilling is dominated by terrigenous clastics [*Westbrook et al.*, 1994]. The lower $\sim$1 km of the section, as identified along strike to the south outboard of the Astoria Fan and correlated using seismic data [*Westbrook et al.*, 1994], is composed of an upper, sand-rich distal fan facies overlying a mud- and clay-rich basin facies. Plate convergence, resolved normal to the trench, is approximately 3.7 cm yr^{-1}. The northern Cascadia accretionary complex is characterized by a relatively steep taper angle of $\sim$8–10° [*Westbrook et al.*, 1994; *Hyndman et al.*, 1993a].

[54] The narrow ($\sim$20–25 km wide) accretionary complex offshore Mexico drilled during DSDP Leg 66 is formed from a $\sim$670- to 800-m-thick incoming sediment section. The incoming sediment is composed of a $\sim$170-m-thick pelagic facies overlain by a $\sim$625-m-thick coarse-sand-rich fan deposit [*J. C. Moore et al.*, 1982]. The thickness of the fan deposits is related to nearby canyons and varies significantly along strike, decreasing to near zero $\sim$50 km from the drilled transect. Unrecovered sediment in the trench-fan facies is assumed to be dominated by very coarse sands because there is no indication of other lithologies in this unit [*Watkins et al.*, 1981]. The convergence rate is 7.0 cm yr^{-1}, and the taper angle of the accretionary complex in this area is $\sim$16°.

[55] Observed changes in taper angle within individual accretionary complexes are also consistent with our model results. For example, at the eastern Nankai accretionary complex along the Muroto transect, the taper angle increases from $\sim$4° to $\sim$8° approximately 35 km landward of the trench. This zone of increased taper angle, termed the "large thrust slice zone" [*Moore et al.*, 2001; *Ashi and Taira*, 1992], corresponds to a portion of the prism composed of thick, strongly stratified sediment packages thought to be sand-dominated. Interestingly, this region also corresponds to decreased underconsolidation within underthrust sediment, as inferred from porosities estimated from seismic reflection amplitudes at the prism-underthrust boundary [*Bangs et al.*, 2004]. In the context of our modeling results, a decrease in pore pressure at $\sim$35 km landward of the trench as inferred from the change in taper angle and seismic amplitudes would be expected because higher-permeability sands comprise the wedge arcward of this point [*Moore et al.*, 2001]. Similarly, an increase in the taper angle of the Makran accretionary complex $\sim$70 km landward of the trench coincides with the appearance of seismically imaged thrust faults that cut down to the basal décollement. *Fowler et al.* [1985] interpret this coincident change in slope and fault geometry to reflect more efficient drainage of the accretionary complex and underthrust section caused by throughgoing faults which effectively increase the bulk permeability of the wedge. However, similar observations of steepening taper angle 40–60 km landward of the trench at the northern Antilles accretionary complex are not clearly tied to changes in accreted sediment type or to increased faulting [*Westbrook et al.*, 1988].

[56] At margins where drilling has not been conducted, observations from geophysical surveys are in general agreement with the trend predicted by our models. At the Chile margin, where turbidite deposits comprise a large fraction of the incoming sediment, steep taper angles are reported. At

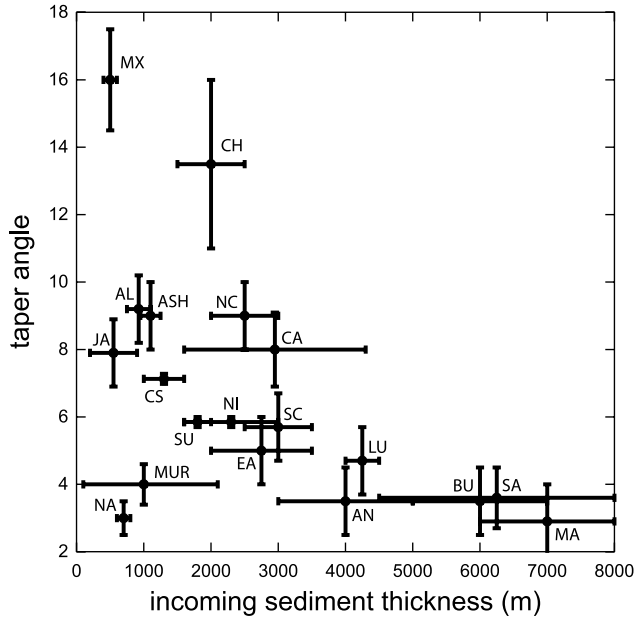

Figure 10. Taper angles of active accretionary complexes versus reported thickness of incoming sediment and using abbreviations in Table 3.

margins where turbidites comprise a moderate proportion of the sediments (Central Aleutian, Java, Nicobar, Sunda, and Sumatra), lower taper angles are reported. For example, at southern Chile, the 2-km-thick incoming section is composed almost entirely of turbidites, and the narrow accretionary complex exhibits a relatively steep 13.5° taper angle [*Polonia et al.*, 1999; *Laursen et al.*, 2002]. Along a transect of the Central Aleutian subduction zone and incoming plate at ~160° W, the incoming sediments range from 750 to 1000 m thick, with up to 850 m of turbidites derived from the Zodiac Fan; the wedge along this transect is characterized by a moderately steep taper angle of 9.2° [*Stevenson et al.*, 1983]. Offshore Java, the incoming sediment section is 200–900 m thick and is composed of more than 50% silt/sand turbidites, and the small accretionary wedge there exhibits a 7.9° taper [*G. F. Moore et al.*, 1980, 1982]. Offshore Central Sumatra, Nicobar, and Sunda, reported incoming sediment thicknesses are 1000–1600 m, 1600–3000 m, and 1600–2000 m, respectively, and the incoming section is composed of a few hundred meters thick hemipelagic drape overlain by turbidites [*Moore et al.*, 1980]. Although the thickness of turbidites varies along strike as a function of canyon discharge and basement relief, they generally comprise >50% of the total sediment; these accretionary complexes also maintain moderate taper angles (5.9–7.1°) [*Moore et al.*, 1980].

[57] Permeability values derived from both inverse hydrologic modeling studies [e.g., *Wang*, 1994; *Bekins et al.*, 1995; *Saffer and Bekins*, 1998] and direct measurements on core samples obtained by drilling at Nankai, northern Antilles, and Cascadia [*Taylor and Leonard*, 1990; *Taylor and Fisher*, 1993; *Carson and Westbrook*, 1995; *Giambalvo et al.*, 2000] are also in good agreement with our results (Figure 9b). Although the inverse modeling results are not entirely independent of the analysis presented here (because the models are constrained, at least in part, by the requirement of elevated pore pressure along the wedge base), it is noteworthy that permeabilities constrained by models that incorporate site-specific porosity-depth trends, plate convergence rates, and sediment thicknesses for eastern Nankai, northern Antilles, and Cascadia are all consistent with our results (Figure 9b). This agreement also suggests that variation in the porosity-depth relationship has only a small effect on pore pressures (as noted in section 2.1.2).

4.1.2. Effects of Sediment Thickness

[58] Sediment thickness exerts a strong control on pore pressure and thus taper angle (Figures 6c and 7c). Larger incoming sediment thickness increases hydrologic forcing (Γ) (Figure 3c), increases drainage path length (L), and decreases hydraulic conductivity (K) by driving lower average porosity. All of these effects result in higher pore pressures. Large sediment thickness probably has additional effects not incorporated into our models, because high temperatures within a thick sediment section would tend to decrease permeability even further by driving diagenesis and low-grade metamorphism [e.g., *Kato et al.*, 2004]. In addition, large trench sediment thicknesses may be related to high sedimentation rates; this could further enhance the effect of sediment thickness reported here by generating significantly elevated pore pressures even before sediments are incorporated into the accretionary wedge [e.g., *Le Pichon et al.*, 1993].

[59] A compilation of available data from active accretionary convergent margins is in excellent agreement with our results, in that increased sediment thickness is strongly correlated with decreased taper angle (Figure 10 and Table 3) [e.g., *Clift and Vannucchi*, 2004; *Lallemand et al.*, 1994]. Notably, considerable variability in taper angle is observed at margins with thinner sediment sections (<3 km), but generally not for those with thicker sediment (Figure 10). As discussed above, we attribute this difference to the increased importance of lithologic variability within thin sediment sections; the relative proportions of lower-permeability hemipelagic and pelagic clay-rich sediment is more variable in these cases and this variability is expressed as discussed in section 4.1.1 (compare Figures 9 and 10). For thicker incoming sediment, the section is typically dominated by trench turbidites (fine-grained sediment comprises a very small fraction of the section) and the effect of sediment thickness on pore pressure is more uniformly expressed (Figure 10).

[60] All known active margins characterized by sediment thicknesses >4000 m are characterized by small taper angles. At the Makran accretionary prism, formed by the subduction of the Arabian Plate beneath the Eurasian Plate at 3–5 cm yr^{-1} [*White*, 1984], the incoming sediment section is 6–7 km thick and is thought to be composed of ~4 km of turbidites overlain by ~3 km of sands [*White and Louden*, 1982; *Kopp et al.*, 2000; *Kukowski et al.*, 2001], although the lower ~4 km has been alternatively interpreted to consist of interbedded turbidites and hemipelagic sediment [*Schlüter et al.*, 2002a]. Where penetrated by drilling well outboard and west of the trench, the distal turbidite facies consists mainly of silts and muds with some sands [*Prell et al.*, 1987]. The taper angle of the Makran accretionary wedge is 2.0–4.5°, suggesting high pore pressure [e.g., *White and Louden*, 1982]. High pore pressure is also

inferred from active mud volcanism near the trench, and from drilling results onshore in coastal Makran [*Minshull and White*, 1984]. Similarly, the southernmost Antilles accretionary complex is formed from a ~6- to 7-km-thick incoming sediment section, thought to be dominated by sand-rich turbidites shed from the Orinoco River [e.g., *Speed et al.*, 1984; *Faugeres et al.*, 1993; *Westbrook*, 1982], and is characterized by a taper angle of 3.6° [e.g., *Ferguson et al.*, 1993; *Brown and Westbrook*, 1988; *Lallemand et al.*, 1994]. As at Makran, mud volcanism near the trench indicates high pore pressures [e.g., *Speed et al.*, 1984], and a pattern of decreasing mud volcano activity to the north follows the thinning of the incoming sediment section with increased distance from the South American continent [*Brown and Westbrook*, 1988]. In both cases, the thick incoming sedimentary section can drive high pore pressures, despite potentially high sediment permeability (e.g., Figure 6c).

[61] The Luzon, Andaman, and Burma accretionary complexes also fit this pattern, with thick incoming sediment sections and shallow taper angles. The Luzon accretionary complex is characterized by sediment thickness of 4000–4500 m, and a taper angle of 4.7° [*Hayes and Lewis*, 1984; *Karig and Sharman*, 1975]. *Hayes and Lewis* [1984] infer from seismic reflection data that the hemipelagic drape immediately overlying the ocean crust is relatively thin, and the section is dominantly composed of thick turbidites. *G. F. Moore et al.* [1980, 1982] reported incoming sediment thicknesses of 3000–5000 m and 5000–7000 m for the Andaman and Burma margins, respectively. In these two regions, the taper of the accretionary complex is ~3.5°. In both locations, the section is composed of a thin 200- to 400-m-thick hemipelagic drape overlain by three thick turbidite sequences derived from the Himalaya [*G. F. Moore et al.*, 1980, 1982].

[62] Several margins characterized by intermediate sediment thicknesses (northern and southern Cascadia, central Aleutians (172–176°W), eastern Aleutians (148–150°W), Nicobar, Sunda) exhibit intermediate taper angles (Figure 10 and Table 3). The incoming sediment at these margins is dominantly composed of turbidites [e.g., *McCarthy and Scholl*, 1985; *G. F. Moore et al.*, 1980, 1982], although the section at Cascadia also includes an appreciable thickness of hemipelagic sediments [e.g., *Underwood*, 2006]. At margins where sediment thickness is lower, lithologic variability probably plays a significant role in affecting taper angle; thus taper angles exhibit more scatter than for larger sediment thicknesses (Figure 10; see discussion in section 4.1.1). Nonetheless, at margins with small thicknesses of incoming sediment composed dominantly of turbidites such as Mexico and Chile, which are lithologically most comparable to margins with thicker sections, large taper angles are observed [e.g., *J. C. Moore et al.*, 1982; *Polonia et al.*, 1999].

[63] At the Cascadia accretionary wedge offshore southern Oregon and Vancouver taper angles are 8–10°, in contrast to the portion offshore northern Oregon and Central Washington where the taper angle is 3–6° [*Flueh et al.*, 1998]. The smaller taper angle in the central section corresponds to a zone of landward verging thrusts in the accretionary complex, which have been interpreted as evidence for higher pore pressures [e.g., *MacKay*, 1995; *Seeley*, 1977]. Although this region has not been drilled, the zone of landward vergence has been correlated with the location of two large submarine fans, the Nitinat and Astoria fans [*Underwood*, 2002, 2006]. The accretion of a thicker sediment section offshore Washington, if in fact the case, is also generally consistent with model predictions of higher pore pressure and smaller taper angle for thicker sediment sections [e.g., *Fisher et al.*, 1999]. At the northern Sumatra margin, *Karig et al.* [1980] noted a correlation between accretion of a thinner sediment section in the past, and increased taper angle in the rear of the accretionary wedge; although highly speculative, this observation may reflect lower pore pressures in the rear of the complex related to the thinner incoming section.

[64] Previous interpretations of existing data [*Clift and Vannucchi*, 2004; *Kopf and Brown*, 2003] have suggested that plate convergence rate is the primary control on taper, with increased plate convergence rate leading to larger taper angles, opposite to the trend shown by our modeling results. However, sediment thickness and plate convergence rate are tightly correlated (higher convergence rates lead to smaller thicknesses) [*Clift and Vannucchi*, 2004, Figure 10]. Indeed, *Clift and Vannucchi* [2004] also note the strong correlation between sediment thickness and taper angle. When a more complete and updated data set is considered that includes (1) all modern accretionary complexes, including Mexico and Chile, (2) well documented along-strike variations at individual margins, and (3) more recently reported geometries for Chile and Makran, the relationship between sediment thickness and taper is even more pronounced (Figure 10 and Table 3). For active accretionary complexes, when the observed range of plate convergence rates (~1.5–6 cm/yr) and thicknesses (500–7000 m) are considered in light of our modeling results (comparison of Figures 7c and 7e), it is clear that the effect of thickness should be dominant.

[65] In contrast to previous work [*Clift and Vannucchi*, 2004; *Kopf and Brown*, 2003], we suggest that rapid plate rate is not the causal mechanism for observed steep taper angles. We base this argument on (1) the lack of a physical mechanism to explain how high plate convergence can cause steeper wedges and (2) the strong correlation between plate convergence and sediment thickness, combined with our modeling results, which provide a viable mechanism to explain the observed relationship. Although high plate convergence rates drive high pore pressures in our simulations [e.g., *Saffer and Bekins*, 2002], we argue that this effect is not manifested at active margins because the effect of sediment thickness is more important.

4.1.3. Implications for Other Tectonic Settings and Processes

[66] We suggest that the conceptual model advanced here can be applied to a wide range of geologic settings. We expect that rocks characterized by small hydrologic forcing and high permeability, such as crystalline rock in intracratonic settings, should be well drained and obey Byerlee's law [*Hickman*, 1991]. This concept has been used to argue that high-permeability faults may actually maintain high frictional strength in the crust by maintaining hydrostatic pore pressures [*Townend and Zoback*, 2000]. In comparison, rocks subject to high deformation rates, rapid hydrologic forcing, and having low permeability will be poorly

drained and may deform under low deviatoric stress. For example, *Irwin and Barnes* [1975] suggest that rapid hydrologic forcing driven by metamorphism of Franciscan rocks, combined with the low permeability of overlying layered sediment, results in low strength and aseismic behavior along segments of the San Andreas Fault. As shown here, this idea is consistent with observations and theoretical predictions of elevated pore pressure at subduction zones. Such a model may also explain deformation at low deviatoric stress in other geologic environments where hydrologic forcing is high relative to permeability.

[67] Our modeling results may also have implications for understanding processes controlling the updip limit of seismogenic behavior along subduction faults. As noted in previous work, for fault zone materials capable of unstable slip (i.e., characterized by velocity-weakening frictional behavior), increased effective stress leads to an increased tendency for instability [e.g., *Scholz*, 1998]. If near-lithostatic pore pressure is maintained to great distances from the trench, effective stress will be low and the tendency for unstable slip decreased; in contrast, if the wedge base is well drained, effective stress will be higher and the tendency for unstable slip increased [e.g., *Scholz*, 1998; *Moore and Saffer*, 2001]. Following this logic, our modeling results suggest that for margins characterized by low-permeability or thick incoming sediment, the updip limit of seismogenesis may tend to be farther from the trench than at margins characterized by high-permeability or thin incoming sediment.

4.2. Limitations of First-Order Analysis

4.2.1. Porosity Loss and Compaction

[68] Variations in the prescribed rate of porosity loss with depth and distance from the trench in our model are of minor importance in estimating the fluid sources [e.g., *Bekins and Dreiss*, 1992; *Le Pichon et al.*, 1990]. However, it is still important to note that the rate of sediment consolidation is coupled to pore pressures and permeability through mean effective stress. This effect is not captured in our model simulations, because porosity loss is prescribed rather than explicitly coupled to fluid flow [e.g., *Screaton et al.*, 1990; *Wang*, 1994]. Low sediment permeability should retard consolidation, resulting in slower porosity loss (thus driving smaller fluid sources than estimated in our simulations), whereas high permeability should allow rapid consolidation (thus driving larger fluid sources) [e.g., *Ge and Garven*, 1992; *Shi and Wang*, 1988; *Davis*, 1996]. We simulated delayed consolidation corresponding to observed porosities and presumably appropriate for overpressures at eastern Nankai. This falls in the middle of the range of taper angles and sediment composition of most of our simulations. If permeabilities are higher, the sediment can drain more easily, leading to higher fluid sources, but it follows from the assumption of drainage that the higher sources do not lead to higher pressures. Higher sources require higher permeabilities to maintain the same pore pressure. This means that for the steep taper angles, the required permeabilities may be somewhat higher than our model results. Conversely, if sediment is even more underconsolidated than at Nankai, fluid sources are lower. Again it follows from the assumption of extreme underconsolidation that the lower sources do not lead to lower pressures. The lower sources require lower permeabilities to maintain the same overpressure. This means that for shallow taper angles, the required permeabilities may be somewhat lower than our results. It is most important to note that underconsolidation increases permeability of hemipelagic sediment by at most a factor of $\sim$20 [*Zwart et al.*, 1997]. In contrast, a change from clay-rich sediment to sand increases permeability by 5 orders of magnitude (Figure 4).

[69] On the basis of work by *Bekins and Dreiss* [1992], we suggest that these effects would result in only a minor modification to our results. Furthermore, the observation that detailed inverse modeling studies of Nankai, northern Antilles, and Cascadia are consistent with our model, despite different site-specific porosity-depth curves used for each margin, implies that the effects of varying the porosity-depth expression are small.

4.2.2. Spatially Variable Pore Pressure Ratio and Wedge Criticality

[70] As discussed above, we define stability criteria for critically tapered wedges assuming that $\lambda = \lambda_b$. Although modeled pore pressure ratio typically varies both laterally and with depth in the model domain [e.g., *Saffer and Bekins*, 2002], using these stability criteria allows a viable first-order evaluation of wedge criticality. In general, the effects of laterally and depth-variable pore pressure ratio are secondary to the effects of its overall magnitude [e.g., *Breen and Orange*, 1992; *Zhao et al.*, 1986]. In some studies, where λ_b is systematically and significantly different from λ, wedge stability can be evaluated by relating the two [e.g., *Saffer*, 2002; *Matmon and Bekins*, 2006]. For most model simulations we find that λ_b is slightly greater than λ, and the maximum variability in simulated values of λ within the model domain is $<20-30\%$. The magnitude of variation in simulated pore pressure allows a decrease in wedge taper angle by a maximum of $\sim 1.5^\circ$. Moreover, as shown in equation (1a), a smaller taper angle may result from either higher values of λ_b, or lower values of μ_b. Thus the range of stability criteria we consider effectively captures a suite of scenarios in which the wedge base is weaker than the wedge itself, including the case where $\mu_b = \mu$ (as supported by laboratory measurements of frictional strength [*Brown et al.*, 2003]) and $\lambda_b > \lambda$.

[71] At locations where stratigraphy results in systematic down-section trends in permeability, this first-order evaluation of criticality may need refinement. For example, if underthrust sediment is characterized by low permeability, and the wedge is composed of high-permeability sediment, a resulting pattern of $\lambda_b \gg \lambda$ would allow lower taper angles than noted here. However, we note that in many cases where drilling has penetrated the incoming sediment, such as the northern Antilles and western Nankai, this stratigraphic pattern is not observed [e.g., *Mascle et al.*, 1988; *Moore et al.*, 2001].

4.2.3. Time-Dependent Variations in Permeability

[72] Permeability in tectonically active environments may be increased by deformation, through hydraulic fracture, formation of mud volcanoes, or by brittle failure. Likewise, it may decrease over time due to decreasing pore pressure (increased effective stress) or mineral precipitation. The effects of deformation on permeability are accounted for in our study only by permeability reduction with porosity loss and by inclusion of a high-permeability décollement.

Incorporation of additional effects is beyond the scope of our current work. However, we note that unless faults and other discrete failure structures are closely spaced, the permeability of undisturbed sediment matrix should control fluid escape from the compacting sediment [e.g., *Neuzil*, 1994].

[73] Permeability of faults is known to vary as a function of effective stress [e.g., *Fisher and Zwart*, 1996]. The transient hydrologic behavior of faults in accretionary complexes has been explored in previous numerical modeling studies, using constraints from downhole geochemistry [e.g., *Bekins et al.*, 1995; *Saffer and Bekins*, 1998] and thermal data [e.g., *Screaton and Ge*, 1997; *Henry*, 2000]. Here, we do not consider the effects of time-dependent permeability and fluid pressure variations, because such variations probably occur over temporal and spatial scales that are small relative to the age and size of the complex [e.g., *Bekins et al.*, 1995].

5. Conclusions

[74] Unlike existing mechanical models of accretionary complexes, which treat pore pressure as an independent parameter that controls critical taper angle, we note that pore pressure results from a dynamic balance between a set of more fundamental factors. These include permeability structure, sediment thickness, and plate convergence rate. We demonstrate that permeability (governed largely by lithology), hydrologic forcing (controlled by geometry, sediment thickness, and plate convergence rate), and drainage path length exert a primary control on spatially and temporally averaged pore pressure. The net result is that these factors control the mechanical failure of the wedge and décollement, and therefore the critical taper angle.

[75] We show that accretionary wedges characterized by low-permeability or thick incoming sediment sections should exhibit small critical taper angles, whereas those characterized by high-permeability or thin incoming sediment sections should exhibit large taper angles. On the basis of our analysis, we suggest that along-strike variations in sediment lithology or thickness may profoundly influence the geometry and mechanical behavior of accretionary complexes. Likewise, variations in incoming sediment thickness or composition over time will force the accretionary complex to readjust until a new dynamic balance is reached, and may also result in changes in taper angle downdip within an individual accretionary complex. Existing data from active accretionary complexes are broadly consistent with the conceptual model that taper angle reflects a dynamic balance between hydrologic forcing and pore pressure diffusion (Figure 8) and are highly consistent with our modeling results (Figures 9–10). The importance of hydrologic processes on tectonics, as illustrated for accretionary complexes here, implies that the frictional strength of the brittle crust, and possibly the updip limit of seismogenesis, should be strongly influenced by rock permeability and hydrologic forcing.

[76] **Acknowledgments.** We thank Greg Moore, Chris Neuzil, Elizabeth Screaton, and two anonymous reviewers for constructive comments that have greatly improved this manuscript. Peter Flemings, Casey Moore, and Homa Lee provided helpful discussions and critical reviews of earlier drafts of the manuscript. This work was supported by a National Research Council Associateship and NSF grant OCE-0241482 to Saffer.

References

Ashi, J., and A. Taira (1992), Structure of the Nankai accretionary prism as revealed from IZANAGI sidescan imagery and multichannel seismic reflection profiling, *Island Arc*, *1*, 104–115.

Athy, L. F. (1930), Density, porosity, and compaction of sedimentary rocks, *Am. Assoc. Petrol. Geol. Bull.*, *14*, 1–24.

Bangs, N., et al. (2004), Evolution of the Nankai Trough décollement zone from the trench into the seismogenic zone: Inferences from 3-D seismic reflection imaging, *Geology*, *32*, 273–276.

Behrmann, J. H., and A. Kopf (1993), Textures and microfabrics in fine-grained muds and mudstones from site 808, Nankai accretionary prism, *Proc. Ocean Drill. Program Sci. Results*, *131*, 45–55.

Bekins, B. A., and S. J. Dreiss (1992), A simplified analysis of parameters controlling dewatering in accretionary prisms, *Earth Planet. Sci. Lett.*, *109*, 275–287.

Bekins, B. A., A. McCaffrey, and S. J. Dreiss (1995), Episodic and constant flow models for the origin of low-chloride waters in a modern accretionary complex, *Water Resour. Res.*, *31*, 3205–3215.

Bray, C. J., and D. E. Karig (1985), Porosity of sediments in accretionary prisms and some implications for dewatering processes, *J. Geophys. Res.*, *90*, 768–778.

Breen, N., and D. L. Orange (1992), The effects of fluid escape on accretionary wedges: 1. Variable porosity and wedge convexity, *J. Geophys. Res.*, *97*, 9265–9275.

Brown, K., and G. K. Westbrook (1988), Mud diapirism and subcretion in the Barbados Ridge accretionary complex: The role of fluids in accretionary processes, *Tectonics*, *7*, 613–640.

Brown, K. M., et al. (1994), Heterogeneous hydrofracture development and accretionary fault dynamics, *Geology*, *22*, 259–262.

Brown, K. M., et al. (2003), Compositional and fluid pressure controls on the state of stress on the Nankai subduction thrust: A weak plate boundary, *Earth Planet. Sci. Lett.*, *214*, 589–603.

Byrne, T., and D. Fisher (1990), Evidence for a weak and overpressured decollement beneath sediment-dominated accretionary prisms, *J. Geophys. Res.*, *95*, 9081–9097.

Byrne, T., et al. (1993), Deformation structures and fluid flow in the toe region of the Nankai accretionary prism, *Proc. Ocean Drill. Program Sci. Results*, *131*, 83–101.

Carson, B., and E. J. Screaton (1998), Fluid flow in accretionary prisms: Evidence for focused, time-variable discharge, *Rev. Geophys.*, *36*, 329–351.

Carson, B., and G. K. Westbrook (1995), Modern fluid flow in the Cascadia accretionary wedge: A synthesis, *Proc. Ocean Drill. Program Sci. Results*, *146*, 413–424.

Chapple, W. M. (1978), Mechanics of thin-skinned fold-and-thrust belts, *Geol. Soc. Am. Bull.*, *89*, 1189–1198.

Clift, P., and P. Vannucchi (2004), Controls on tectonic accretion versus erosion in subduction zones: Implications for the origin and recycling of the continental crust, *Rev. Geophys.*, *42*, RG2001, doi:10.1029/2003RG000127.

Cochrane, G. R., J. C. Moore, M. E. MacKay, and G. F. Moore (1994), Velocity and inferred porosity model of the Oregon accretionary prism from multichannel seismic reflection data: Implications on sediment dewatering and overpressure, *J. Geophys. Res.*, *99*, 7033–7043.

Dahlen, F. A. (1984), Noncohesive critical Coulomb wedges; an exact solution, *J. Geophys. Res.*, *89*, 10,125–10,133.

Davis, D., J. Suppe, and F. A. Dahlen (1983), Mechanics of fold-and-thrust belts and accretionary wedges, *J. Geophys. Res.*, *88*, 1153–1172.

Davis, D. M. (1984), The compressive mechanics of accretionary wedges applied to the Leg 78A study area near Barbados, *Initial Rep. Deep Sea Drill. Proj.*, *78A*, 559–569.

Davis, D. M. (1996), Accretionary mechanics with properties that vary in space and time, in *Subduction: Top to Bottom*, *Geophys. Monogr. Ser.*, vol. 96, edited by G. E. Bebout et al., pp. 39–48, AGU, Washington, D. C.

Davis, D. M., and R. von Huene (1987), Inferences on sediment strength and fault friction from structures at the Aleutian Trench, *Geology*, *15*, 517–522.

Dixon, T. H., et al. (1998), Relative motion between the Caribbean and North American plates and related boundary zone deformation from a decade of GPS observations, *J. Geophys. Res.*, *103*, 15,157–15,182.

Faugeres, J. C., et al. (1993), Quaternary sandy deposits and canyons on the Venezuelan margin and south Barbados accretionary prism, *Mar. Geol.*, *110*, 115–142.

Ferguson, I. J., et al. (1993), Heat flow and thermal models of the Barbados Ridge accretionary complex, *J. Geophys. Res.*, *98*, 4121–4142.

Fisher, A. T., and M. W. Hounslow (1990), Transient fluid flow through the toe of the Barbados accretionary complex: Constraints from Ocean Drilling Program Leg 110 heat flow studies and simple models, *J. Geophys. Res.*, *95*, 8845–8858.

Fisher, A. T., and G. Zwart (1996), Relation between permeability and effective stress along a plate-boundary fault, Barbados accretionary complex, *Geology*, *24*, 307–310.

Fisher, M. A., et al. (1999), Geologic processes of accretion in the Cascadia subduction zone west of Washington State, *Geodynamics*, *27*, 277–288.

Flueh, E. R., et al. (1998), New seismic images of the Cascadia subduction zone from Cruise SO108; ORWELL, *Tectonophysics*, *293*, 69–84.

Fowler, S. R., R. S. White, and K. E. Louden (1985), Sediment dewatering in the Makran accretionary prism, *Earth Planet. Sci. Lett.*, *75*, 427–438.

Ge, S., and G. Garven (1992), Hydromechanical modeling of tectonically driven groundwater flow with application to the Arkoma foreland basin, *J. Geophys. Res.*, *97*, 9119–9144.

Gerdom, M., A. M. Trehu, E. R. Flueh, and D. Klaeschen (2000), The continental margin off Oregon from seismic investigations, *Tectonophysics*, *329*, 79–97.

Giambalvo, E. R., et al. (2000), Origin of elevated sediment permeability in a hydrothermal seepage zone, eastern flank of the Juan de Fuca Ridge, and implications for transport of fluid and heat, *J. Geophys. Res.*, *105*, 913–928.

Gieskes, J. M., P. Vrolijk, and G. Blanc (1990), Hydrogeochemistry of the northern Barbados Accretionary complex transect: Ocean Drilling Program Leg 110, *J. Geophys. Res.*, *95*, 8809–8818.

Gulick, S. P. S., N. L. B. Bangs, T. H. Shipley, Y. Nakamura, G. Moore, and S. Kuramoto (2004), Three-dimensional architecture of the Nankai accretionary prism's imbricate thrust zone off Cape Muroto, Japan: Prism reconstruction via en echelon thrust propagation, *J. Geophys. Res.*, *109*, B02105, doi:10.1029/2003JB002654.

Hayes, D., and S. D. Lewis (1984), A geophysical study of the Manila Trench, Luzon, Philippines: 1. Crustal structure, gravity, and regional tectonic evolution, *J. Geophys. Res.*, *89*, 9171–9195.

Henry, P. (2000), Fluid flow at the toe of the Barbados accretionary wedge constrained by thermal, chemical, and hydrogeologic observations and models, *J. Geophys. Res.*, *105*, 25,855–25,872.

Henry, P., et al. (2002), Surface expression of fluid venting at the toe of the Nankai wedge and implications for flow paths, *Mar. Geol.*, *187*, 119–143.

Henry, P., L. Jouniaux, E. J. Screaton, S. Hunze, and D. M. Saffer (2003), Anisotropy of electrical conductivity record of initial strain at the toe of the Nankai accretionary wedge, *J. Geophys. Res.*, *108*(B9), 2407, doi:10.1029/2002JB002287.

Hickman, S. H. (1991), Stress in the lithosphere and the strength of active faults, *U.S. Natl. Rep. Int. Union Geod. Geophys. 1987–1990*, *Rev. Geophys.*, *29*, 759–775.

Housen, B. A., et al. (1996), Strain decoupling across the decollement of the Barbados accretionary prism, *Geology*, *24*, 127–130.

Hubbert, M. K., and W. W. Rubey (1959), Role of fluid pressure in mechanics of overthrust faulting, *Geol. Soc. Am. Bull.*, *70*, 115–166.

Hyndman, R. D., et al. (1993a), Velocity, porosity, and pore-fluid loss from the Nankai subduction zone accretionary prism, *Proc. Ocean Drill. Program Sci. Results*, *131*, 211–219.

Hyndman, R. D., K. Wang, T. Yuan, and G. D. Spence (1993b), Tectonic sediment thickening, fluid expulsion, and the thermal regime of subduction zone accretionary prisms; the Cascadia margin off Vancouver Island, *J. Geophys. Res.*, *98*, 21,865–21,876.

Irwin, W. P., and I. Barnes (1975), Effect of geologic structure and metamorphic fluids on seismic behavior of the San Andreas Fault system in central and northern California, *Geology*, *3*, 713–716.

Ito, T., S. Yoshioka, and S. Miyazaki (1999), Interplate coupling in southwest Japan deduced from inversion analysis of GPS data, *Phys. Earth Planet. Inter.*, *115*, 17–34.

Karig, D. E. (1985), The framework of deformation in the Nankai Trough, *Initial Rep. Deep Sea Drill. Proj.*, *87*, 927–940.

Karig, D. E. (1986), Physical properties and mechanical state of accreted sediments in the Nankai Trough, southwest Japan arc, *Mem. Geol. Soc. Am.*, *166*, 117–132.

Karig, D. E., and G. F. Sharman III (1975), Subduction and accretion in trenches, *Geol. Soc. Am. Bull.*, *86*, 377–389.

Karig, D. E., M. B. Lawrence, G. F. Moore, and J. R. Curray (1980), Structural framework of the fore-arc basin, NW Sumatra, *J. Geol. Soc. London*, *137*, 77–91.

Kastner, M., et al. (1993), Geochemical and isotopic evidence for fluid flow in the western Nankai subduction zone, Japan, *Proc. Ocean Drill. Program Sci. Results*, *131*, 397–413.

Kato, A., A. Sakaguchi, S. Yoshida, H. Yamaguchi, and Y. Kaneda (2004), Permeability structure around an ancient exhumed subduction zone fault, *Geophys. Res. Lett.*, *31*, L06602, doi:10.1029/2003GL019183.

Kimura, G., et al. (Eds.) (1997), *Proceedings of the Ocean Drilling Program*, *Initial Reports*, vol. 170, 458 pp., Ocean Drill. Program, College Station, Tex.

Kopf, A., and K. M. Brown (2003), Friction experiments on saturated sediments and their implications for the stress state of the Nankai and Barbados subduction thrusts, *Mar. Geol.*, *202*, 193–210.

Kopp, C., et al. (2000), Structure of the Makran subduction zone from wide-angle and reflection seismic data, *Tectonophysics*, *329*, 171–191.

Kopp, H., E. R. Flueh, D. Klaeschen, J. Bialas, and C. Reichert (2001), Crustal structure of the central Sunda margin at the onset of subduction, *Geophys. J. Int.*, *147*, 449–474.

Kukowski, N., et al. (2001), Morphotectonics and mechanics of the central Makran accretionary wedge off Pakistan, *Mar. Geol.*, *173*, 1–19.

Kulm, L. D., et al. (1973), *Initial Reports of the Deep Sea Drilling Project*, vol. 18, 1077 pp., U.S. Govt. Print. Off., Washington, D. C.

Lallemand, S., and X. Le Pichon (1987), Coulomb wedge model applied to the subduction of seamounts in the Japan Trench, *Geology*, *15*, 1065–1069.

Lallemand, S. E., P. Schnurle, and J. Malavielle (1994), Coulomb theory applied to accretionary and nonaccretionary wedges: Possible causes for tectonic erosion and/or frontal accretion, *J. Geophys. Res.*, *99*, 12,033–12,055.

Lamb, S., and P. Davis (2003), Cenozoic climate change as a possible cause for the rise of the Andes, *Nature*, *425*, 792–797.

Laursen, J., D. W. Scholl, and R. von Huene (2002), Neotectonic deformation of the central Chile margin: Deepwater forearc basin formation in response to hot spot ridge and seamount subduction, *Tectonics*, *21*(5), 1038, doi:10.1029/2001TC901023.

Le Pichon, X., P. Henry, and S. Lallemant (1990), Water flow in the Barbados accretionary complex, *J. Geophys. Res.*, *95*, 8945–8967.

Le Pichon, X., P. Henry, and S. Lallemant (1993), Accretion and erosion in subduction zones: The role of fluids, *Annu. Rev. Earth Planet. Sci.*, *21*, 307–331.

Logan, J. M., and K. A. Rauenzahn (1987), Frictional dependence of gouge mixtures of quartz and montmorillonite on velocity, composition, and fabric, *Tectonophysics*, *144*, 87–108.

MacKay, M. E. (1995), Structural variation and landward vergence at the toe of the Oregon accretionary prism, *Tectonics*, *14*, 1309–1320.

MacKay, M. E., et al. (1992), Landward vergence and oblique structural trends in the Oregon margin accretionary prism: Implications and effect on fluid flow, *Earth Planet. Sci. Lett.*, *109*, 477–491.

Mascle, A., et al. (1988), *Proceedings of the Ocean Drilling Program*, *Initial Reports, Part A*, vol. 110, 603 pp., Ocean Drill. Program, College Station, Tex.

Matmon, D., and B. A. Bekins (2006), Hydromechanics of a high taper angle, low permeability prism: A case study from Peru, *J. Geophys. Res.*, doi:10.1029/2005JB003697, in press.

McCaffrey, A. M. (1994), The impact of the smectite to illite transformation on fluid flow and solute transport in the Barbados accretionary complex, M.S. thesis, Univ. of Calif., Santa Cruz.

McCarthy, J., and D. W. Scholl (1985), Mechanisms of subduction accretion along the central Aleutian Trench, *Geol. Soc. Am. Bull.*, *96*, 691–701.

McMillen, K. J., R. H. Enkebol, J. C. Moore, T. H. Shipley, and J. W. Ladd (1982), Sedimentation and tectonics, Middle America Trench, southern Mexico and Guatemala, in *Trench and Forearc Geology*, edited by J. K. Leggett, *Geol. Soc. Spec. Publ.*, *10*, 107–119.

Minshull, T., and R. White (1984), Sediment compaction and fluid migration in the Makran accretionary prism, *J. Geophys. Res.*, *94*, 7387–7402.

Minshull, T. A., and R. White (1989), Sediment compaction and fluid migration in the Makran accretionary prism, *J. Geophys. Res.*, *94*, 7387–7402.

Miyazaki, S., and K. Heki (2001), Crustal velocity field of southwest Japan: Subduction and arc-arc collision, *J. Geophys. Res.*, *106*, 4305–4326.

Moore, G. F., J. R. Curray, D. G. Moore, and D. E. Karig (1980), Variations in geological structure along the Sunda Fore Arc, northeastern Indian Ocean, in *The Tectonic and Geologic Evolution of Southeast Asian Seas and Islands*, *Geophys. Monogr. Ser.*, vol. 23, edited by D. E. Hayes, pp. 145–160, Washington, D. C.

Moore, G. F., J. R. Curray, and F. J. Emmel (1982), Sedimentation in the Sunda Trench and forearc region, in *Trench-Forearc Geology*, edited by J. K. Leggett, *Geol. Soc. Spec. Publ.*, *10*, 245–258.

Moore, G. F., et al. (1990), Structure of the Nankai Trough accretionary zone from multichannel seismic reflection data, *J. Geophys. Res.*, *95*, 8753–8765.

Moore, G. F., et al. (2001), *Proceedings of the Ocean Drilling Program*, *Initial Reports* [CD-ROM], vol. 190, Ocean Drill. Program, College Station, Tex.

Moore, J. C., and B. Biju-Duval (1984), Tectonic synthesis, Deep Sea Drilling Project Leg 78A; structural evolution of offscraped and underthrust sediment, northern Barbados Ridge complex, *Initial Rep. Deep Sea Drill. Proj.*, *78A–78B*, 601–621.

Moore, J. C., and D. M. Saffer (2001), Updip limit of the seismogenic zone beneath the accretionary prism of southwest Japan: An effect of diagenetic to low-grade metamorphic processes and increasing effective stress, *Geology*, *29*, 183–186.

Moore, J. C., and H. Tobin (1997), Estimated fluid pressures of the Barbados accretionary prism and adjacent sediments, *Proc. Ocean Drill. Program Sci. Results*, *156*, 229–238.

Moore, J. C., and P. Vrolijk (1992), Fluids in accretionary prisms, *Rev. Geophys.*, *30*, 113–135.

Moore, J. C., et al. (1982), Facies belts of Middle America Trench and forearc region, southern Mexico: Results from Leg 66 DSDP, Trench-forearc geology: sedimentation and tectonics on modern and ancient active plate margins, conference, in *Trench-Forearc Geology*, edited by J. K. Leggett, *Geol. Soc. Spec. Publ.*, *10*, 77–94.

Moore, J. C., et al. (1991), EDGE deep seismic reflection transect of the eastern Aleutian arc-trench layered lower crust reveals underplating and continental growth, *Geology*, *19*, 420–424.

Moran-Zenteno, D. J., P. Corona-Chavez, and G. Tolson (1996), Uplift and subduction erosion in southwestern Mexico since the Oligocene: Pluton geobarometry constraints, *Earth Planet. Sci. Lett.*, *141*, 51–65.

Morgan, J. K., and D. E. Karig (1993), Ductile strains in clay-rich sediment from Hole 808C; preliminary results using X-ray pole figure goniometry, *Proc. Ocean Drill. Program Sci. Results*, *131*, 141–155.

Morris, J. D., et al. (2003), *Proceedings of the Ocean Drilling Program*, *Initial Reports* [CD-ROM], vol. 205, 611 pp., Ocean Drill. Program, College Station, Tex.

Nelson, P. H. (1994), Permeability-porosity relationships in sedimentary rocks, *Log Anal.*, 38–62.

Neuzil, C. E. (1994), How permeable are clays and shales?, *Water Resour. Res.*, *30*, 145–150.

Neuzil, C. E. (1995), Abnormal pressures as hydrodynamic phenomena, *Am. J. Sci.*, *295*, 742–786.

Ogawa, Y., K. Fujioka, K. Fujikura, and Y. Iwabuchi (1996), En echelon patterns of Calyptogena colonies in the Japan Trench, *Geology*, *24*, 807–810.

Platt, J. P. (1986), Dynamics of orogenic wedges and the uplift of high-pressure metamorphic rocks, *Geol. Soc. Am. Bull.*, *97*, 1037–1053.

Polonia, A., et al. (1999), Structural variability at the active continental margin off southernmost Chile, *Geodynamics*, *27*, 277–288.

Prell, W. L., et al. (1987), *Proceedings of the Ocean Drilling Program*, *Initial Reports*, vol. 117, 1236 pp., Ocean Drill. Program, College Station, Tex.

Revil, A., and L. M. Cathles (2002), Fluid transport by solitary waves along growing faults: A field example from the South Eugene Island Basin, Gulf of Mexico, *Earth Planet. Sci. Lett.*, *202*, 321–335.

Saffer, D. M. (2002), Differences in taper angle along strike of the Nankai accretionary complex: A consequence of lithostratigraphy?, *Eos Trans. AGU*, *83*(47), Fall Meet. Suppl., Abstract H22E-09.

Saffer, D. M. (2003), Pore pressure development and progressive dewatering in underthrust sediments at the Costa Rican subduction margin: Comparison with northern Barbados and Nankai, *J. Geophys. Res.*, *108*(B5), 2261, doi:10.1029/2002JB001787.

Saffer, D. M., and B. A. Bekins (1998), Episodic fluid flow in the Nankai accretionary complex: Timescale, geochemistry, flow rates, and fluid budget, *J. Geophys. Res.*, *103*, 30,351–30,371.

Saffer, D. M., and B. A. Bekins (2002), Hydrologic controls on the morphology and mechanics of accretionary wedges and thrust belts, *Geology*, *30*, 271–274.

Schlüter, H. U., et al. (2002a), The Makran accretionary wedge: Sediment thickness and ages and the origin of mud volcanoes, *Mar. Geol.*, *185*, 219–232.

Schlüter, H. U., C. Gaedicke, H. A. Roeser, B. Schreckenberger, H. Meyer, C. Reichert, Y. Djajadihardja, and A. Prexl (2002b), Tectonic features of the southern Sumatra-western Java forearc of Indonesia, *Tectonics*, *21*(5), 1047, doi:10.1029/2001TC901048.

Scholz, C. H. (1998), Earthquakes and friction laws, *Nature*, *391*, 37–42.

Screaton, E. J., and S. Ge (1997), An assessment of along-strike fluid and heat transport within the Barbados Ridge accretionary complex: Results of preliminary modeling, *Geophys. Res. Lett.*, *24*, 3085–3088.

Screaton, E. J., D. R. Wuthritch, and S. J. Dreiss (1990), Permeabilities, fluid pressures, and flow rates in the Barbados ridge complex, *J. Geophys. Res.*, *95*, 8997–9007.

Screaton, E. J., D. M. Saffer, P. Henry, S. Hunze, and Leg 190 Shipboard Scientific Party (2002), Porosity loss within underthrust sediment of the Nankai accretionary complex: Implications for overpressures, *Geology*, *30*, 19–22.

Seeley, D. R. (1977), The significance of landward vergence and oblique structural trends on trench inner slopes, in *Island Arcs, Deep Sea Trenches and Back-Arc Basins*, *Maurice Ewing Ser.*, vol. 1, edited by M. Talwani and W. C. Pitman, pp. 187–198, AGU, Washington, D. C.

Seno, T., S. Stein, and A. E. Gripp (1993), A model for the motion of the Philippine Sea plate consistent with NUVEL-1 and geological data, *J. Geophys. Res.*, *98*, 17,941–17,948.

Shi, Y., and C. Y. Wang (1988), Generation of high pore pressures in accretionary prisms: Inferences from the Barbados subduction complex, *J. Geophys. Res.*, *93*, 8893–8910.

Shipley, T. H., et al. (1994), Seismically inferred dilatancy distribution, northern Barbados ridge décollement: Implications for fluid migration and fault strength, *Geology*, *22*, 411–414.

Shipley, T. H., et al. (1995), *Proceedings of the Ocean Drilling Program*, *Initial Reports*, vol. 156, 301 pp., Ocean Drill. Program, College Station, Tex.

Speed, R. C., et al. (Eds.) (1984), Lesser Antilles Arc and adjacent terranes, in *Atlas 10*, *Reg. Atlas Ser.*, 27 sheets, Ocean Margin Drill. Program, Mar. Sci. Int., Woods Hole, Mass.

Spinelli, G. A., D. M. Saffer, and M. B. Underwood (2006), Hydrogeologic responses to three-dimensional temperature variability, Costa Rica subduction margin, *J. Geophys. Res.*, doi:10.1029/2004JB003436, in press.

Stevenson, A. J., D. W. Scholl, and T. L. Vallier (1983), Tectonic and geologic implications of the Zodiac Fan, Aleutian abyssal plain, northeast Pacific, *Geol. Soc. Am. Bull.*, *94*, 259–273.

Taira, A., et al. (1992), Sediment deformation and hydrogeology of the Nankai Trough accretionary prism: Synthesis of shipboard results of ODP Leg 131, *Earth Planet. Sci. Lett.*, *109*, 431–450.

Taylor, E., and A. T. Fisher (1993), Sediment permeability at the Nankai accretionary prism, site 808, *Proc. Ocean Drill. Program Sci. Results*, *131*, 235–245.

Taylor, E., and J. Leonard (1990), Sediment consolidation and permeability at the Barbados forearc, *Proc. Ocean Drill. Program Sci. Results*, *110*, 289–308.

Townend, J., and M. D. Zoback (2000), How faulting keeps the crust strong, *Geology*, *28*, 399–402.

Ujiie, K., T. Hisamitsu, and A. Taira (2003), Deformation and fluid pressure variation during initiation and evolution of the plate boundary décollement zone in the Nankai accretionary prism, *J. Geophys. Res.*, *108*(B8), 2398, doi:10.1029/2002JB002314.

Underwood, M. B. (2002), Strike-parallel variation in clay mineralogy, fault vergence, and up-dip limits to the seismogenic zone, *Geology*, *30*, 155–158.

Underwood, M. B. (2006), Sediment inputs to subduction zones: Why lithostratigraphy and clay mineralogy matter, in *The Seismogenic Zone of Subduction Thrust Faults*, edited by T. Dixon et al., Columbia Univ. Press, in press.

Underwood, M. B., and S. B. Bachman (1982), Sedimentary facies associations within subduction complexes, in *Trench and Forearc Geology*, edited by J. K. Leggett, *Geol. Soc. Spec. Publ.*, *10*, 537–550.

Underwood, M. B., et al. (1993), Sediment geochemistry, clay mineralogy, and diagenesis: A synthesis of data from leg 131, Nankai Trough, *Proc. Ocean Drill. Program Sci. Results*, *131*, 343–363.

Vannucchi, P., D. W. Scholl, M. Meschede, and K. McDougall (2001), Tectonic erosion and consequent collapse of the Pacific margin of Costa Rica: Combined implications from ODP Leg 170, seismic offshore data, and regional geology of the Nicoya Peninsula, *Tectonics*, *20*, 649–668.

Von Huene, R., and S. Lallemand (1990), Tectonic erosion along the Japan and Peru convergent margins, *Geol. Soc. Am. Bull.*, *102*, 704–720.

Voss, C. I. (1984), A finite element simulation model for saturated-unsaturated, fluid density-dependent groundwater flow with energy transport or chemically reactive single-species solute transport, *U.S. Geol. Surv. Water Resour. Invest. Rep.*, *84-4369*.

Wang, K. (1994), Kinematics of dewatering accretionary prisms, *J. Geophys. Res.*, *99*, 4429–4438.

Watkins, J. S., et al. (1981), *Initial Reports of the Deep Sea Drilling Project*, vol. 66, 864 pp., U.S. Govt. Print. Off., Washington, D. C.

Westbrook, G. K. (1982), The Barbados Ridge Complex; tectonics of a mature forearc system, in *Trench and Forearc Geology*, edited by J. K. Leggett, *Geol. Soc. Spec. Publ.*, *10*, 275–290.

Westbrook, G. K., A. Mascle, and B. Biju-Duval (1984), Geophysics and the structure of the Lesser Antilles forearc, Leg 78, *Initial Rep. Deep Sea Drill. Proj.*, *78*, 39–48.

Westbrook, G. K., J. W. Ladd, P. Buhl, N. Bangs, and G. J. Tiley (1988), Cross section of an accretionary wedge: Barbados Ridge complex, *Geology*, *16*, 631–635.

Westbrook, G. K., et al. (1994), *Proceedings of the Ocean Drilling Program*, *Initial Reports, Part 1*, vol. 146, 611 pp., Ocean Drill. Program, College Station, Tex.

White, R. S. (1984), Active and passive plate boundaries around the Gulf of Oman, north-west Indian Ocean, *Deep Sea Res.*, *31*, 731–745.

White, R. S., and K. E. Louden (1982), The Makran continental margin: structure of a thickly sedimented convergent plate boundary, in *Studies in Continental Geology*, edited by J. S. Watkins and C. L. Drake, *AAPG Mem.*, *34*, 499–518.

Zhang, J. X., D. M. Davis, and T. F. Wong (1993), The brittle-ductile transition in porous sedimentary-rocks: Geological implications for accretionary wedge aseismicity, *J. Struct. Geol.*, *15*, 819–830.

Zhao, W.-L., et al. (1986), Origin of convex accretionary wedges: Evidence from Barbados, *J. Geophys. Res.*, *91*, 10,246–10,258.

Zwart, G., et al. (1997), Evaluation of hydrogeologic properties of the Barbados accretionary prism: A synthesis of Leg 156 results, *Proc. Ocean Drill. Program Sci. Results*, *156*, 303–310.

B. A. Bekins, U.S. Geological Survey, 345 Middlefield Road, MS 496, Menlo Park, CA 94025, USA.

D. M. Saffer, Department of Geosciences, Pennsylvania State University, University Park, PA 16802, USA. (dsaffer@geosc.psu.edu)